Rapid optofluidic detection of biomarkers for traumatic brain injury via surface-enhanced Raman spectroscopy

Rickard, Jonathan; Di Pietro, Valentina; Smith, David; Davies, David; Belli, Tony; Goldberg Oppenheimer, Pola

DOI:
10.1038/s41551-019-0510-4

nature biomedical engineering

Rapid optofluidic detection of biomarkers for traumatic brain injury *via* surface-enhanced Raman spectroscopy

Jonathan J. J. S. Rickard[1,2]*, Valentina Di-Pietro[3,5,] David J. Smith[4], David J. Davies[5], Antonio Belli[3,5] and Pola Goldberg Oppenheimer[1,6]*

[1] School of Chemical Engineering, College of Engineering and Physical Science, University of Birmingham, Edgbaston, Birmingham, B15 2TT, UK
[2] Department of Physics, Cavendish Laboratory, University of Cambridge, JJ Thomson Avenue, Cambridge, CB3 0HE, UK
[3] NIHR Surgical Reconstruction and Microbiology Research Centre, University of Birmingham, Birmingham, B15 2TT, UK
[4] School of Mathematics, College of Engineering and Physical Science, University of Birmingham, Edgbaston, B15 2TT, UK
[5] Department of Neuroscience and Ophthalmology, Institute of Inflammation and Ageing, National Institute for Health Research, University of Birmingham, B15 2TH, UK
[6] Healthcare Technologies Institute, Trauma Management Healthcare Technology Co-operative, University Hospitals Birmingham, NHS Foundation Trust, Queen Elizabeth Hospital Birmingham, Mindelsohn Way, Birmingham, B15 2PR, UK

* Corresponding authors, jjr1001@cam.ac.uk ; GoldberP@bham.ac.uk

Current technologies for the point-of-care diagnosis of traumatic brain injury (TBI) lack sensitivity, require specialist handling or involve complicated and costly procedures. Here, we report the development and testing of an optofluidic device for the rapid and label-free detection, *via* surface-enhanced Raman scattering (SERS), of picomolar concentrations of biomarkers for TBI in biofluids. The device's SERS-active substrate consists of electrohydrodynamically fabricated submicrometre pillars covered with a plasmon-active nanometric gold layer and integrated in an optofluidic chip. In particular, we show that the device can detect N-acetylasparate in finger-prick blood samples from TBI patients, and that the biomarker is released immediately from the central nervous system after TBI. The simplicity, sensitivity and robustness of SERS-integrated optofluidic technology might eventually help the triaging of TBI patients and assist clinical decision-making at point-of-care settings.

One-sentence editorial summary (to appear right below the article's title on the journal's website):
An optofluidic device rapidly detects, *via* surface-enhanced Raman scattering, picomolar concentrations of biomarkers for traumatic brain injury in finger-prick blood samples from patients.

In emergency-care practice, life-critical decisions must be made within a period of minutes which influence patients' prognosis and the efficacy of treatment. Currently, over half of major brain trauma patients are over-triaged, straining healthcare resources and third are under-triaged, overlooking a significant injury burden.[1-3] Confounding factors present during the initial out-of-hospital assessment contact such as, hypotension or hypoxia, intoxication and early intubation represent a significant barrier not only to diagnosis, but to injury severity stratification.

The diagnosis of traumatic brain injury (TBI) in such cases is confirmed radiologically after admission to hospital or clinically, when sedation is stopped and the appropriate neurological function is absent. This may occur several days later thus, missing the critical window for early intervention, be it with current or future therapeutic measures. [4, 5] Stratification of TBI heavily relies on neurological imaging and invasive neuromonitoring, which are typically applied to support diagnosis and therapy. Computerised tomography (CT) scan is the current 'gold-standard' for imaging in the acute care phase, whilst magnetic resonance imaging (MRI) and its advanced applications, such as (H)-magnetic resonance spectroscopy (H^1-MRS) and diffusion tensor imaging, can provide additional information about the injury and potential for recovery. [6-10] However, these methods are not only resource-intensive and impractical in the critically injured individual but also, only feasible in a hospital setting and once the patient has been stabilised. There is, therefore, a growing interest in TBI biomarkers to guide clinical decision making, particularly focussing on the early stages, when timely treatment is critical. [11-13] A range of known central nervous system biomarkers are present in the cerebrospinal fluid (CSF), the composition of which reflects biochemical changes that occur in the brain.[14] CSF however, has to be collected by a lumbar puncture, which is often unsafe in TBI patients and unsuitable for point-of-care (PoC) testing. No technology currently exists for timely diagnosis of neurological damage with sufficient accuracy to enable stratification of patients at risk of deterioration in the acute setting. The stratification of injury severity, and its relationship to the morbidity and mortality of the head injured patient is of a particular importance in the current TBI management, due to the paucity of effective objective measures. Such a tool would not only represent a useful aid in the formulation of current management plans but, it may also serve as a clear objective grading tool for which the administration of therapies may be directed. Previously tested therapeutics that have proved ineffective in the clinical setting [15] (despite promising pre-clinical data) may have reached these conclusions due to the sub-optimal disease severity quantification. This therefore, may represent a 'current day' equivalent of the observed ineffectiveness of surgical interventions in trials prior to the universal adoption of the Glasgow Coma Scale [16] as the standard method of clinically stratifying the severity of TBI. [17]

The use of biofluid-based diagnostic methods can offer clear advantages for the PoC diagnosis since the collection of blood samples is a standard procedure in routine clinical practise. While some molecules are highly-expressed in the central nervous system (CNS), key-challenges associated with the use of blood-biomarkers for TBI diagnostics, include considerably lower concentrations than in CSF, due to their dilution in the blood volume, the effect of the blood-brain-barrier and the effect of clearance of certain molecules from blood *via* the liver or kidneys. Over the last decade, several candidate biomarkers have emerged for clinical manifestations of TBI and associated neurodegenerative conditions (Supplementary Table 1), [18-26] which have been shown to correlate with severity of neurotrauma in the hospital care environment *e.g.,* lipoproteins, [27] glial-fibrillary acidic protein (GFAP), neuron-specific enolase (NSE) and S100B, [28-31] yet, their value is unclear in the earliest, pre-hospital setting. While demonstrating correlation with trauma severity and holding potential diagnostic, prognostic and stratification value, these biomarkers are released into the body fluids in miniscule amounts and are undetectable at early stages with available biochemical techniques with sufficient timeliness and sensitivity at an affordable cost. Analysis is predominantly carried out in specialised laboratories, using mainly high-performance chromatography, mass spectrometry or enzyme-linked immunosorbent assay (ELISA), requiring expensive labels for each target biomarker with time-to-results in the range of several hours or even days and requiring complex equipment, not suitable for PoC.

N-acetylasparate (NAA) is a highly abundant molecule found exclusively within neurological tissue synthesised from aspartic acid and acetyl-coenzyme A within mitochondria. [32] Its precise functions are not clearly understood however, its abundance in cell bodies together with a number of observational relationships have led to its development as a directly or indirectly measured marker of brain health. Within the acute phase of severe TBI, depletion in directly measured NAA *via* microdialysis has demonstrated strong correlation with

injury severity (relating to both radiological, surgical and physiological findings), together with poor prognosis and outcome prediction. [33, 34] Its agreement with other standard clinical microdialasate derived parameters, [35] and their established role in measuring metabolic health, further reinforces a fundamental role in oxidative metabolism. Its depletion within the context of metabolic crisis in the sever TBI has also been confirmed radiologically using H^1-MRS. [36-39] The timeframe in which these radiological observations are made is considerably further from the point of injury (mean: 41 days 38), this is due, in part, to the practical and safety aspect of individuals undergoing long scanning protocols in isolation. This cumulative, clinically derived evidence builds a picture of a molecule critical and specific to neurological function that depletes rapidly following TBI. Its rapid initial reduction from brain tissue would theoretically lead to a spike in concentration within other body compartments during its metabolism and excretion, as the sudden observable reduction in the initial phases 34 are not likely to be due to a reduction in production due to the neurological injury alone. This concept forms the foundation of this investigation. Like many other TBI biomarkers, extracranial injuries may contribute to the NAA elevations after polytrauma *e.g.,* mast cells or peripheral nerve injury. However, given the abundance of this compound in the CNS compared to other tissues, it is likely that the brain would overshadow other potential sources. Clinical studies would be needed to elucidate this more accurately.

Optical methods provide a route to the miniaturisation of sensing devices. Surface enhanced Raman scattering (SERS) is a highly sensitive spectroscopic technique [40-49] enabling detection down to single molecule level *via* enhancement of localized optical-fields on metallic sub-microstructures, which can be tuned by manipulation of the surface roughness and architecture at the sub-micron level. [50-53] It offers distinct advantages over other spectroscopic methods for sensing including, immediate detection of analytes without complex sample-preparation and undergoes no photobleaching. It is also capable of detecting multiple analytes simultaneously due to the narrow bandwidth of fingerprints, reducing the spectral overlap. [54-56] SERS is the only detection technique that can be deployed out of a laboratory setting without a significant loss in performance and is capable of rapid sensing with considerably lower detection limits than currently exploited methods. [57-62] This unique set of attributes makes it well suited to address the challenges associated with PoC diagnostics as practical and sensitive detection of biochemical markers. One of the key challenges of SERS however, is the fabrication of noble-metallic structures that are highly reproducible and sensitive to the target molecules. The substrate on which SERS is performed is often the critical component for successful detection. [53, 63-69] Reliable, cost-effective and consistent fabrication of sensitive, tuneable, stable and reproducible SERS-active structures still remains a considerable challenge. Any imperfections in substrates have a significant effect on the ultimate response. The high enhancement is usually achieved by using random metallic nanoparticles, from which only a minute fraction exhibit SERS activity thus, substantially affecting the signal, exhibiting high-sample detection variability, aggregation and poor batch-to-batch repeatability. [63, 64, 70-73] Graphene based substrates are being broadly explored as potential SERS surfaces exhibiting good enhancements with improved selectivity. Nevertheless, these are often achieved with surfaces modifications and, they are yet to be optimised for uniformity and improved reproducibility as well as sensitivity for achieving trace level detection. [41, 74] Furthermore, not only are substrates with tuneable surface plasmon resonances matching the excitation lasers needed to gain the highest enhancement, a challenging task for lab-on-a-chip systems but also to date, optofluidic systems have been largely based on external, bulky components requiring alignment expertise to collect the signal, rendering these not portable, expensive and incapable of rapid-detection. In contrast, sub-microstructures on substrates can intrinsically overcome this problem for stable SERS measurements.

Here we report a non-labelled device technology for the detection of neurological biomarkers in blood plasma at minute concentrations. Our development combines controllable and reproducible electrohydrodynamically fabricated optofluidic lab-on-a-chip, microengineered for enabling sensitive and consistent SERS detection in an integrated sensor for timely diagnosis and triaging of TBI scenarios. Biomarkers indicative of severe TBI (*e.g.,* NAA, GFAP and S100B) are shown to be successfully detected at trace levels from blood plasma, either individually or as a panel from miniscule biofluids volumes. Providing the opportunity to measure disease biomarkers, paves the way for further clinical utility and validation studies that would have not previously been possible. Integration of our microengineered optofluidic chip with the portable Raman system provides portable device with combined simplicity, sensitivity and reproducibility and holds a great potential to help triaging the TBI patients to assist clinical decision-making in the pre-hospital settings. Detection of TBI-indicative biomarkers at PoC in conjunction with clinical evaluation can provide critical information for the stratification of patients and enable a sophisticated assessment of the primary TBI akin to a CT scan, while reducing the cost

and radiation exposure. It further lays a groundwork for monitoring brain injury and alerts of subsequent risk of neurological deterioration that would help avoid long-term deficits and morbidity.

Results and discussion

We have developed lithographically defined lab-on-a-chip which is more stable than nanoparticle-based systems, offering more degrees of freedom in the design and tuning of structural parameters. It enables reproducible, multiplex and molecule specific SERS enhancement, providing technology for rapid detection of biomarkers at picomolar concentrations from blood plasma at the PoC. Reproducible electrohydrodynamic microlithography encompasses induction of amplified instabilities in thin nanofilms (Fig.1a).

Assembling a microcapacitor-like device with a thin polymer layer on a bottom electrode opposed by a second electrode, with an applied voltage gives rise to a high electric field across the dielectric material and air gap. The subsequent dielectric discontinuity at the interface in the capacitor triggers the formation of displacement charges, coupling to the electric field and causing a destabilizing electrostatic pressure, which eventually overcomes the stabilising forces of the *Laplace* pressure, yielding energetically more favourable configurations. Typically, the experimental set-up of the electrohydrodynamic patterning comprises a slight misalignment of the capacitor plates resulting in a wedge geometry with a variation in electrodes spacing ranging from 100nm to 1µm across for a 1cm wide sample (Fig. 1a, ii) and thus, yielding the lateral variation in the resultant pillar's aspect ratio (Fig. 1a, ii, inset and Fig. 1b, i). We have established that the highest enhancement factor of the SERS active pillars is achieved when the aspect ratio is 0.8 (Fig. 1a, iii and Fig. 1b, ii) [66, 75] and subsequently, designed and fabricated a dedicated top electrode with protruding pillars of 625nm in diameter. Since, such a top electrode in a capacitor-like device generates laterally varying electric field, the redistributing material is drawn towards the protrusions, where the electrostatic pressure is the highest and the electrohydrodynamic destabilisation process is the fastest, faithfully reproducing the imposed structure (Fig. 1a, iv and Fig. 1b, iii). Corresponding AFM and SEM images are shown in Fig. 1b.

Microengineered device is based on controllable electrohydrodynamically fabricated sub-microstructured substrates *via* a dedicated rig combining a micromanipulator and piezo actuator for the finest adjustments, enabling a parallel capacitor-like electrohydrodynamic patterning set-up for homogenous fabrication of submicron pillars (Fig. 1c). The micro-lithographic set-up is designed to allow for several degrees of freedom of movement and therefore, well-aligned parallel positioning of the top and bottom electrodes, (Methods and Supplementary Fig.S1) yielding the integrity and accuracy of the inter-capacitor distance down to submicron scale and thus, fabrication of very accurate and highly-reproducible SERS-active substrates. Tuneability of the structural dimensions of the fabricated substrates, which are conformally covered by a plasmon-active gold nanolayer to enhance the electromagnetic field (Fig. 1b iv, 1d, inset i and Supplementary Fig. S2), is enabled *via* the independent control of the lithographic experimental parameters *e.g.,* inter-electrode spacing, electric field and initial film thickness. The controllable aspect ratio and its effect on strength of plasmon resonances and SERS, allows the optimization of substrates for different laser excitation wavelengths (Supplementary Fig.S3).

The gold coated (h_{pillar} = 500±12nm, gold thickness = 23nm) pillar arrays were numerically simulated by a two-dimensional model using a finite-element method, where a plane-wave is incident normal to the substrate with a linear polarization perpendicular to the top edge (Supplementary Fig. S4). Modelling of electromagnetic wave interactions revealed enhanced electromagnetic fields predominantly localized in the region on top of the pillars (Fig. 1d, inset ii). While the structures couple light into plasmon-polariton and propagating plasmon resonances by diffraction, the controlled periodicity renders the adjacent pillars not plasmonically coupled to each other, generating a strong localization on top of the structures and consequently, high-fields and SERS enhancements, arising almost exclusively from a single structure (Fig. 1d, inset iii), each of which can act as an individual detection centre. The coupling between plasmons on the pillars results in red-shifted apex plasmons. For the incident excitation, the SERS signals which occur at these red-shifted wavelengths are Stokes shifted and therefore, enhanced on the pillar region. Such polarization sensitive anistropic localization of plasmons and SERS signals offers the possibility of selective detection at the single structure level. The simulation of the intensity distribution demonstrates that localized surface plasmon resonance intensity in period of 800nm is the strongest when the incident laser wavelength is 785nm, indicating that the optical enhancement on the surface is mainly due to plasmon coupling, which could be tuned by variation of the

periodic topologies and spacing and with these substrates, SERS signals can be achieved from concentrations as low as parts per billion.

SERS spectra of benzenethiol molecules on the fabricated substrates across several indiscriminate areas on each substrate demonstrate repeatable signal and substrate consistency (Fig. 1d). Raman signals from different pillars on the SERS substrates are highly-uniform, exhibiting signal reproducibility and repeatability (Supplementary Figs.S5-S8). Reproducibility of the enhanced signal of fingerprint signatures was established by measuring at three random locations on each substrate, fabricated individually using the dedicated rig (Fig. 2a). The reproducibility coefficient (Supplementary Fig.S9) was found to be such that the absolute difference between any three future measurements made on a particular substrate are estimated to be no greater than 4.3% on 95% of occasions. Furthermore, the correlated SERS enhancement factor (EF) calculation results show that 89% of values are narrowly distributed around the average of $7.73\times10^9 \pm 2.94\times10^9$ (Fig. 2a). We therefore, expect that the difference in the EF as measured between the different substrates to lie between 7.30×10^9 and 7.80×10^9 for 95% of the future measurements. The enhancement factor is normalized by the spot size and since the SERS activity is localized at the surface structure, it stems only from a small fraction of the sample area. Reproducible electrohydrodynamically fabricated chip offers a robust substrate for high cross-section based SERS detection.

The SERS substrates were further used to characterise the fingerprint spectra and to determine the lowest detectable concentrations of three representative biomarkers signposted to correlate with TBI including, the NAA, S100B and GFAP. The characteristic peaks of each biomarker were monitored (Supplementary Fig.S10 and Fig.S11) and a linear relationship was observed with a good correlation between biomarker concentrations (100nM to 1fM) and Raman intensity, with R^2=0.9994, 0.9989 and 0.9755, for the NAA, S100B and GFAP, respectively (Fig. 2b and Supplementary Fig. S8). The calculated limit of detection (LoD) was established to be 0.021 pg/mL (0.12pM) for the NAA, 3.99pg/mL (0.19pM) for S100B and 3.35pg/mL (0.02pM) for the GFAP and the limit of quantitation (LoQ) for the NAA was found to be 0.067pg/mL (0.38pM) and 10pg/mL (0.19pM) for the GFAP.

Multivariate analysis on the multiplex biomarker set revealed principal component loadings with clearly separated clusters that recapitulate the fine spectral differences of the molecular fingerprinting spectra, effectively discriminating the three TBI indicative biomarkers (Fig. 2b, inset). On the basis of the reproducible SERS identification, spectral database was constructed with different standards to enable identification of TBI-indicative biomarkers. Initially, standard SERS spectra were extracted of the respective pure solution of the NAA, S100B and GFAP (Supplementary Fig. S11), allowing the generation of a specific and unique fingerprint spectrum for each standard, which were further used for the barcoding. The finger print spectra were barcoded with the representative Raman bands of the highest intensity and spectral differences compared for the healthy volunteers (HV) and sever TBI (sTBI). The SERS spectra of the NAA (Supplementary Fig.S11, a), GFAP (Supplementary Fig.S11, b) and S100B (Supplementary Fig.S11, c), each showed a number of characteristic bands, which were then used for their identification. Multiplex barcoding of a panel of three biomarkers from a complex biological matrix, based on their unique SERS signatures and the computational algorithm, enables selective and sensitive method for detection of TBI biomarkers. The electrohydrodynamically fabricated substrates can be stored for more than six months without performance degradation, important for employing these for rapid, cost-effective PoC diagnostics.

Microengineered platforms have further been used to analyse clinically relevant samples. The biomarkers were measured in clinical blood plasma, collected as part of the Golden-Hour (GH) study (Supplementary Fig.S12) (Ethics Ref. 13/WA/0399), providing blood samples from TBI and non-TBI patients (Table 1). Overall, a total of 221 measurements were collected from blood plasma samples of GH group, the 23 healthy volunteers (HV) acting as a control group (ReCoS Study, Ethics Ref. 11-0429AP28), the extracranial injury (EC) only group and 35 sTBI subjects including, the sTBI combined with EC (sTBI+EC) sub-group (Methods).

The first blood sample collection was carried out by the ambulance team at the roadside within minutes from the point of injury (t=0) and further samples were collected at various time points post TBI: t=4-12h, 48. Following the molecular peak signatures corresponding to specific structural and composition information, we spiked the blood plasma samples of healthy patients with the TBI-indicative biomarkers (Supplementary

Fig.S13). The samples were then analysed with and without the spiked biomarker to test the recovery. Recovery observed for the spike is nearly identical, within the experimental error, to the recovery obtained for the analyte prepared in standard diluents, validating the sample matrices for the detection assay.

Wilcoxon rank sum/Mann-Whitney U test of TBI biomarkers for healthy control group, HV and TBI patients yielded significantly different spectra between the sTBI and HV groups when analysed for each biomarker (Supplementary Fig. S14, a-c). An interesting facet of the data set was the strong correlation observed between the levels of the NAA detected with GFAP and S100B (Supplementary Fig. S14, d-e). Since these are established markers of neurological injury and although not robustly specific to TBI, represent a reasonable measure of neuro cytological injury, it is expected that the quantity of NAA release will relate directly to the burden of cytological injury in a similar way and therefore, these two quantities would closely correlate. With the difference between the GH and HV groups being the most significant for the NAA biomarker (Fig. 2c) specifically differentiating between TBI and non-TBI patients, we have further predominantly focussed on studying and detecting the NAA as a primary TBI biomarker.

NAA is one of the most abundant molecules present in the CNS which, (Supplementary Table 2) due to its exclusive localization in neurons, reflects the oxidative metabolic status of neurons and axons in the brain. It is considered as a marker for neuronal health and viability and thus, constitutes a measure of neuronal compromise. As previously discussed, its depletion has been observed in the brain of patients with TBI by a number of direct and indirect methods including *in-vivo* H^1-MRI or by post-mortem histopathological evidence. [76-80] This has signposted the NAA as a biomarker for detecting TBI early in the patient journey, and potentially allowing the monitoring its progression (*via* secondary injurious development) and identifying the optimal timing and nature of possible therapies. Nevertheless, NAA can also be found in peripheral nervous tissue, mast cells and retina. [36, 37] Within the context of polytrauma or multi-system trauma, particularly those involving the spine, brachial plexus or eye caution should be used before relying on concentrations of peripheral NAA to quantify brain tissue injury burden. Since NAA is very abundant in the CNS compared to other tissues, we hypothesise that contribution of extracranial injuries to NAA levels after polytrauma would be relatively small, or perhaps even negligible, compared to the brain. This seems to be corroborated by our findings after comparing different injury cohorts (Fig. 2d and Table 1). It is also found in abnormally high levels in the serum of individuals suffering from conditions such as Canavan disease. Here in particular, its detection was only possible due to the very high concentration accumulated in the brain and followed by a substantial excretion into the blood. [81, 82] Furthermore, clinical evidence suggests that high NAA levels found in CSF provide a very sensitive predictor of neuronal damage and mortality. They may relate to excretion of NAA into the blood circulation, where the levels are considerably diluted, following increased metabolite from damaged neurons and in physiological conditions low serum NAA levels might be related to its rapid filtration in the kidneys. [83, 84] It is important to note, that brain tissue NAA depletion is seen in a number of different forms of acute brain injury. [85] However, in the context of trauma as a mechanism of injury, *i.e.,* a road traffic accident, NAA measurement in the peripheral suggests TBI as the cause.

We have subsequently employed the feature selection method to enable Raman classification accuracy,[86, 87] *via* establishing an optimal, smallest subset of peaks allowing the discard of the least important features. Initially, the significant peaks of the NAA spectra were selected for classification and the calculated coefficients between the reference peak and every chosen feature allowed to reduce the number of candidates, selecting the most frequently appearing peaks (Supplementary Figs.S15 and S16). By calculating the highest *a posteriori* probability (Methods), [42, 88, 89] the primary significant peaks, yielding the most discriminality from the pre-processed spectrum, were chosen as the feature candidates for classification, with the most discriminating peak selected as a reference feature at 1420cm^{-1}. Fig. 2d shows the matrices of multilayer perceptions with distribution of the highest performing selected features of sTBI, sTBI+EC and HV with each axis corresponding to the intensity or ratio of maximum value at each selected peak, providing clear decision boundaries for the patients with and without TBI. SERS spectra of the blood plasma taken from patients diagnosed with sTBI and sTBI+EC at t=0 in comparison to the healthy control group reveal distinct spectral features including, the increase in the intensity ratio of peaks at 717cm^{-1} and 1010cm^{-1} and the appearance of additional peaks or increase in their intensity at 682, 930, 1168, 1292, 1420, 1517 and 1623cm^{-1} (Fig. 2d, inset). Specific differences of certain selected features originate from biochemical variations in blood plasma post TBI are reflected in the SERS spectra indicating the molecular composition changes (Fig. 1e). The intensity of the peak

at 682cm^{-1} is attributed to the *wagging* of C=O and *twisting* of –OH bonds in the N-acetyl groups whereas, the peak at 717cm^{-1} originates from the *stretching* of CαC bonds as well as the *deformation* of the O-H groups. The peaks at and between 1010cm^{-1}, 1168cm^{-1} are assigned to the out-of-plane *rocking* mode of the CH_3, *twisting* of the CH_2 and the *wagging* on the C=O amides and the N-H vibrations in the NH-C=O-CH_3 group at 1517cm^{-1} are characteristic of N-acetyl groups, which are significantly elevated in the blood plasma samples derived from sTBI patients and absent or at considerably lower concentration in the healthy control samples. The intensity of the peak at 1420cm^{-1} originates from the acetylamide in the CH_3-NH-C=O of the N-acetyl asymmetric *vib* CH_3 deformations. The selected feature bands closely reflect the NAA molecular structure and its variations at the earliest stages of TBI (Figs. 2d, inset and e). At the t_{TBI}=0, peaks originating from NAA become more pronounced in the SERS spectra, indicating that in the earliest stages post TBI, the concentration of NAA increases in blood plasma providing a pre-diagnostic value to the in-hospital histopathological outcomes. SERS vibrational signatures of blood plasma in Fig. 2e, i-iii from the healthy cohort, sTBI clinical samples and sTBI with EC show prominent variability between sTBI and the non-TBI patients. The characteristic peaks from sTBI and sTBI+EC spectra are then compared with the fingerprint SERS spectra of the NAA (Fig. 2e, iv) with selected features of five peak ratios and three peak intensities (highlighted as dotted lines) form the multilayer perception classification yielding the SERS barcode for TBI detection *via* an indicative biomarker.

Next, we carried out NAA profiling to monitor clinical progression of TBI for more targeted management of secondary brain injury events, which could be linked to episodes of resulting deterioration such as, raised intracranial pressure. [21, 34] Time-dependent SERS spectra of NAA show dynamic fluctuations of neurochemical marker levels over the course of time (Fig. 3) as the NAA is continuously effluxed from neurons into the blood circulation and thus, builds up temporal profiles of extracellular activity during the various phases of TBI. The intensities, I_{1420}/I_{1517} ratio may be used not only for the differentiation of the sTBI but also to monitor the progress post injury as the ratio of the peaks decreases with time depending on the pathological status (Fig. 3a). As TBI occurs clinically, the metabolites and protein contents in the blood increase and the peaks originating from these become more pronounced in the SERS spectra. We observed a temporal correlation to the mean levels of the NAA, which were more than five times higher in sTBI patients at *t*=0 than in the control group, which gradually decreased over the course of 48 hours (Fig. 3b). Therefore, temporal evolution of blood plasma using micro-engineered substrates enables early, more sensitive and repeatable detection of neuormarkers than CT or H^1-MRI for instance, which can only assess the state of the brain at a set moment in time (Fig. 3a, inset). NAA levels were significantly elevated in patients with sTBI immediately after the injury (median: 6.03pg/mL, IQR: 0.52pg/mL, p<0.0010) compared with the control cohort (median: 1.22pg/mL, IQR: 0.45pg/mL) and the EC group (median: 0.85pg/mL, IQR: 0.27pg/mL) (Table 1). We used receiver operating characteristic (ROC) curves to assess the patients profiling data and analyse the ability of NAA to differentiate sTBI patients at various time points after the injury by calculating the area under the curve (AUC) at each time point post TBI plotting the true positive versus the false negative rates (Fig. 3c-e). From the ROC curves we determined the intrinsic classification accuracy of 98.7% for the NAA at *t*=0 (Fig. 3c), 90.9% at *t*=8h (Fig. 3d) and 91.0% at *t*=48h (Fig. 3e), clearly discriminating between sTBI and HV groups and sTBI versus EC patients, which is crucial for classifying traumatic head injuries versus injuries occurring elsewhere in the body.

Molecular fingerprinting based on the microengineered platforms is highly-sensitive and can rapidly detect the indicative biomarkers at the earliest point of interest (Supplementary Table 2) enabling an important diagnostic technology from both therapeutic and prognostic viewpoints. Stratified plasma NAA levels, based on the median values, were higher in sTBI cases than in EC group (Mann-Whitney test) at all three time points with a particularly significant difference at *t*=0, where the NAA concentrations are seven times higher in sTBI versus the extra-cranial injury cases with no overlap in the outliers of the 95% confidence interval of the non-parametric quarter range in comparison to a low number of overlaps with the outliers in the HV group (Fig. 3f-h). Microengineered surfaces enabled detection at pM concentrations, indicating a sharp increase in the NAA levels in blood plasma post TBI, followed by a gradual decrease of the metabolic marker levels, without reaching the corresponding control group values after 48 hours. Our data thus, indicates that following neuro-damage, in particular, at the earliest trauma stages, sTBI events are characterized by a leakage of NAA into the blood stream, highlighting the possibility of detection and diagnosis at the PoC. The time course of NAA in TBI observed in our experiments, with five times higher biomarker levels compared to the healthy controls and

patients with EC trauma at the early stages post injury, indicates a direct correlation to the neuronal damage, implying NAA efflux to the blood stream.

Next, we have studied samples from mild TBI (mTBI) patients (*n*=13) supported by the MRI imaging and the corresponding H^1-MRS and have observed that the levels of blood NAA decreased among mTBI patients, whereas levels of the biomarker increased in sTBI patients (Supplementary Fig.S17). H^1-MRS was undertaken on selected (*n*=6) subjects of the concussion cohort with observably lower concentrations of NAA in blood (Supplementary Fig.S18). The recovered spectroscopic parameters were then compared to an age and sex matched set of non-concussed individuals. The median value for NAA/Choline ratio was higher in the healthy group (4.41 *versus* 1.16) but this was not statistically significant (Mann-Whitney U test, *p*=0.54). Conversely, the NAA/Creatinine ratios were significantly lower in the concussion cohort (Mann-Whitney U test, *p*=0.009). These observations are generally consistent with the blood concentrations of NAA, as they represent a relative reduction in production of NAA due to the concussive insult. These results are to be considered preliminary but, suggest an interesting correlation between the biomarker levels and the cellular mechanisms of injury. The decrease in the NAA ratios on H^1-MRS is attributed to reduced mitochondrial NAA synthesis, which is known to occur in mild TBI, whereas in severe TBI, the late decrease in the NAA ratios is attributed to depletion of the neuronal population. [90-92] This could explain why in mTBI we have recorded a simultaneous drop in blood NAA levels (reduced biosynthesis and/or increased utilisation), whereas in severe TBI, the increase in blood levels can be explained by outflow of NAA from damaged cells. Therefore, potentially, blood NAA levels can be further utilised in the evaluation of the mTBI. Given the limited number of samples, this point can only be speculative and much larger cohorts of TBI patients would be needed to confirm this. Further studies will seek to establish correlation with radiological abnormalities.

Whilst the combination of neurological exam with CT and MRI scans can offer detailed information about a TBI, the presence of confounders, such as alcohol or polytrauma, can prevent neurological assessment at the point-of-care and imaging would not be available until the patient reaches hospital. [93-96] This can lead to misdiagnosis or delayed treatment in the prehospital setting, where most of the acute damage occurs. Pre-hospital confirmation of brain injury would help instigate the correct neuroprotective measures immediately and would help triage the patient appropriately, *e.g.,* direct them to a major trauma centre with neurosurgical facilities as opposed to the local trauma unit. At present, there is no validated biomarker to assist clinical decision-making in the pre-hospital setting, which results in traumatic brain injury being frequently misdiagnosed (over- or under-triage). This justifies the intense quest for a rapid, PoC assessment of TBI in austere environments. While it is very challenging for single biomarker test to address all the issues of this complex field, this study does provide a potential important modality to evaluate TBI in austere settings, which was not previously available. Our technique provides an opportunity to measure TBI-indicative biomolecules, which have convincingly been demonstrated to correlate with tissue injury, neurological dysfunction and recovery in the brain tissue of animals and in human studies using H^1-MRS but were not previously measured in blood. This will pave the way for further confirmatory and clinical utility studies.

We established a quantitative assay which provides discriminative sensitivity to detect target biomarkers with trace level analyte concentrations (Table 1 and Supplementary Fig.S19). Consistent sub-microstructures are highly-uniform, fabricated in a single step process and exhibit high SERS signal enhancement, making the micro-engineered chip well suited for real-time biodiagnostic applications as well as for fundamental studies of biochemical mechanisms involving the detected analytes (Fig. 4). Optofluidic SERS substrates were further integrated within a microfluidic chip and miniaturized Raman optics, providing distinct advantages in delivering affordable, portable and non-invasive neurotrauma-indicative sensing device. Micro-engineered device comprises a spectral detection assay with a disposable integrated optofluidic SERS unit, (Fig. 4e, inset) a portable Raman system for PoC sample analyses, consisting of a 785nm laser, lenses, gold and diachroic mirrors with an echelle spectrometer (Fig. 4c) and a microfluidic chip (Fig. 4b and Supplementary Fig.S20) to rapidly separate plasma from the whole human blood through capillary action and directly filter the plasma to the SERS detection region (Fig. 4b). The whole blood, introduced into the inlet reservoir, (Supplementary Fig.S20, e, g and i) flows along the main capillary channel (110μm width×10μm depth×100mm length) with a lateral velocity of 250±13μm/s and drawn through the cross-flow filter combs, consisting of repetitive arrays of 2μm wide, 200μm long and 1.2μm deep channels, (Supplementary Fig.S20,e and h-l) eliminating the infiltration of red blood cells, with shear stress reducing the flow resistance, while providing a consistent flow rate within

the primary channel, with the separated plasma directed to the detection area (cross-section area of 6×3mm^2) comprised of the integrated SERS structures, in the final optofluidic design. No blood cells are observed in the separated plasma, (Supplementary Fig.S20, j, k and l) indicating high-separation efficiency at flow rate of 1.2μL·h^{-1}, consistent with the previously shown results, where 100% separation efficiency sustained at flow rates below 50μL/h. [97] No dilution of the whole blood further preserves the native biomarker concentrations. The channels twisting are used to draw sample past the filters towards the outlet reservoir for the depleted blood (Supplementary Fig.S20, j). This design allows coupling of the high-capillary pressure between deeper and shallower structures with relatively low flow resistance by means of capillary phenomena, effectively separating small volumes of whole blood in rapid manner. Tailor-made filter combs allow the separating of different constituents of blood into each collection reservoir for SERS analysis and the high sensitivity of the detection technique combined with the small volumes of the microfluidic chip enables that only a drop of blood is sufficient as an input sample volume, [97-105] [106] enabling the use of the finger prick procedure for blood sampling in our system *versus* the alternative need of traditional vein-puncture for blood drawing (Fig. 4b and) Supplementary Fig.S20, i).

The electrohydrodynamically fabricated SERS unit integrated into the optofluidics yields a single lab-on-a-chip for the whole process including processing of the blood sample and biomolecule detection. Biofluid samples are easily introduced into the microfluidic channels where the Raman spectra are acquired while the laser spot is focused on the pillar(s). Only minute volumes are required to obtain the spectrum for the identification of infinitesimal concentrations within a few seconds acquisition time. The acquired SERS are then rapidly compared to the pre-established database and the reference samples. While a significant correlation between plasma NAA levels and TBI progression yields possible prognostic value in patients with TBI prior to secondary impairment, a selective diagnostic blood test can be created based on a comparison of the obtained spectroscopic changes in the blood of the patient under evaluation with a developed library of Raman spectroscopic signatures for TBI and other diseases. Our microengineered technology exhibits attributes complying to the “ASSURED” criteria,[65] which define the diagnostic tests for PoC (Supplementary Table 3).

Outlook

Several optimisation processes and modifications could be further implemented to improve the micro-engineered technology and accelerate its application for clinical use (Supplementary Fig. S21). First, discriminated multiplex detection from complex biofluids can be tackled by applying advanced scanning optics for excitation while controlling a sequential beam focusing on specific pillars of the electrohydrodynamically generated structures. We have therefore, fabricated the next-generation, tuneable structural arrays with slight variations in aspect ratios between the adjacent areas which can further be coupled with advanced optical arrangements and functionalization with different capture molecules on each pillar. Second, we are developing advanced optics system, which will enable individual SERS spectra to be measured from each active region with individual calibration models. In this manner, the concentration of each biomarker will be established independently, offering a biomarker panel to the clinical users. This optics will be integrated in the micro-engineered technology portable reader to enable laser excitation and spectrum measurement from each active region on the SERS substrate independently. The laser beam will be focused to a spot size smaller that the region, confirm it is focused entirely in the required area combined with mechatronics and sequentially, focus the beam in each different region for each biomarker measurement. Subsequently, it will continuously be scanned between the regions of the SERS substrates at high speed using mirrors mounted on galvo-motors, from which the excitation beam will pass through tube and scan lens to the SERS substrate, allowing sub-seconds switching between the differently functionalized SERS areas. The SERS-signal will be recorded in back-scattering geometry using the high numerical aperture scan lens and diverted to the spectrometer from the excitation beam using specially designed sharp edge or holographic notch filters. Importantly, the versatility of our micro-engineered device technology will make it further applicable in many clinical areas and might accelerate the successful early diagnosis of various diseases.

Methods

Rig for the reproducible electrohydrodynamic lithography. In order to carry out the patterning process, a rig was designed to allow for several degrees of freedom of movement and therefore, well-aligned positioning of the top electrode parallel to the bottom thin film. The rig was constructed with a rectangular aluminium (Al) base and protruding through it is a micrometer with a non-rotating head. A copper block was placed on top of

the non-rotating head acting as the bottom substrate support. A vertical glass bar pillar was also attached to the aluminium base-plate, over which a glass arm was clamped. At the end of the arm, which is above the copper bottom substrate support, a rectangular piezo actuator with two microns of movement has been glued using high temperature glue. On both the bottom and top substrate supports, beryllium copper spring clamps, thinner than the height of the silicon substrates were glued to hold the silicon on the edges and allow a bias voltage to be applied to the top and bottom substrates. To allow the substrates to be as parallel as possible the two substrates were brought together by adjusting the micrometer until the substrates were pressing tightly together and subsequently, the copper block was secured by a screw clamp onto the micrometer head. Therefore, once the micrometer was backed away from the top, the gap was precisely parallel. Glass was chosen for the supporting pillar parts as it is an insulator and has a low coefficient of thermal expansion. When the whole device was heated up, the gap could be coarsely adjusted by turning the micrometer followed by the fine adjustment using the piezo actuator. The distance was gauged by measuring the current being drawn between the top and bottom substrates and subsequently, adjusted using the piezo actuator. This gave the gap integrity accuracy down to the nanometre scale.

Fabrication of reproducible electrohydrodynamic SERS substrates. Polystyrene with a molecular weight of 100kg/mol was used as a main polymer for the electrohydrodynamic patterning (Polymer Standards, GmbH) and toluene was used as a main solvent in this process (Fisher Scientific). Highly polished *p*-doped silicon (Si) wafers with <100> crystal orientation (Wafernet, GMBH) were used during the electrohydrodynamic patterning as bottom and top electrodes (X-lith eXtreme Lithography). Initially, a solution of 3wt% polystyrene was prepared and subsequently, filtered through a Teflon filter with a pore diameter of 100nm. Thin films with initial thickness of h were spin-cast onto 1x1cm^2 silicon substrates from polystyrene in toluene solutions. Prior to the spin-coating, the surfaces were cleaned in a 'Piranha' solution consisting of 3:1 H_2SO_4:H_2O_2, (98%):(30%), followed by thorough rinsing with deionised water and drying under nitrogen flow. Furthermore prior to the patterning set-up assembly, all electrodes were subjected to snow-jet cleaning.
To facilitate the release of the patterned substrates, the surface was rendered apolar by surface grafting an octadecyltrichlorosilane (OTS) self-assembled monolayer. The silicon wafers were electrically contacted by sputtering a 100 nm gold layer on the unpolished backside. The whole rig was heated to 170°C, well above the glass transition of the patterned polymer to allow it to flow and the micrometer was adjusted while the rig was hot to give a rough adjustment followed by the fine adjustment of the gap between the top and bottom substrates, achieved using the piezo whilst in-built voltammeter sensor enabled *in-situ* monitoring by measuring the current that was drawn by the rig during the patterning process. This has yielded electrohydrodynamic instabilities, which resulted in patterning of pillars spanning the capacitor gap with very precise and controllable dimensions. At given set-up settings, these can be tuned and highly reproduced from substrate to substrate. The experimental parameters including, the initial film thickness, the inter-electrode gap, the generated electric field inside the capacitor device, the patterning and termination times as well as surface tension, can be all experimentally controlled. All these directly enabled the fine-tuning of the final morphologies for fabricating the optimal SERS active platforms.

Preparation and testing of gold coated SERS substrates. The patterned substrates were coated with a thin nano-gold layer of a thickness of 23.0±1.7nm (Emitech sputter-coater) using a DC argon plasma and a target with purity of 99.999% (Kurt J. Lesker) *via* two subsequent cycles of 30 seconds at 10 mA. The gold deposition was performed onto all of the electrohydrodynamically generated structures and onto polymer films as reference surfaces. This was followed by adsorption of a benzenethiol (Analytical Standard, Sigma-Aldrich) monolayer on the gold coated surfaces from ethanolic solution at varying concentrations.

Numerical modelling. A two-dimensional model using COMSOL Multiphysics v4.3, a commercial finite-element model solver, was constructed to enable parametric studies. The illustration of the model is depicted in Supplementary Figure 3 with the Floquet periodicity boundary conditions applied to the system. The thickness of the gold layer covering the pillars was 23.0nm with the corresponding optical constants of gold and Si, directly depending on the wavelength, were extracted from Johnson *et* al.[46] A *p*-polarized plane wave, travelling normal to the surface, was illuminating the pillars. The refractive index of the polymer and the surrounding medium was set at 1.3 and 1, accordingly. The total width and depth of the model were 500 and 700 nm. Perfectly matched layers were used to absorb the scattered radiation in all directions with a thickness of 50nm. The field intensity was taken either in the middle of the pillars or 1nm away from them. In both cases,

two points were examined, a point at the height of the pillars and in the middle height. The electric field was calculated as a ratio of its value at a given point (1 nm away from the pillar edge) divided by the incident field *i.e.,* $|E|/|E0|$. SERS enhancement was calculated for the excitation wavelength and the measured Raman wavelength: $(|E|\text{Excitation(nm)}/|E0|)^2$ x $(|E|\text{Raman(nm)}/|E0|)^2$. The incident field of wavelengths at 785nm propagates from the top in the (-z) direction with linear polarization in the x-direction. The incident field amplitude was E_0 = 1V/m. The model was solved for the scattered field of the pillars in a vacuum.

Raman spectroscopy setup and SERS measurements. SERS measurements were carried out using micro Raman spectroscopy system with InVia Qontor spectrometer for confocal Raman (Renishaw Plc.) equipped with 514, 633 and 785 nm lasers which was adjusted for optimal throughput, fluorescence control and sensitivity. Standard biomarkers (GFAP, S100B) for individual fingerprint signature studies were acquired from Human ELISA Kit (Abnova). LoDs were determined using the equation of the line obtained from the dilution studies and calculating the LoD as 3 times the STDEV of the blank, derived by the gradient of the straight line and LoQ as $10x\sigma/S$ where, σ is the standard deviation of the response and *S* is the slope of the calibration curve. The spectra were typically acquired at 10s exposure time and a laser power of 1 to 3mW with 785nm laser to avoid photochemical effects in the SERS spectra, sample damage or degradation. SERS maps were generated in a Streamline mode scan with 10s exposure time and 50mW power at 785nm. A 50x objective with a numerical aperture of 0.75 was used for SERS measurements over a range of 500 to 1800cm^{-1} relative to the excitation Raman shift. Optical measurements were carried out with a specially adapted research grade microscope (Leica DM 2700M) equipped with incoherent white light source, allowing confocal measurements with 2.5μm depth resolution. The spectra were normalized with respect to those recorded on flat gold or gold covered flat polymer film surfaces. An intelligent fitting filter was applied for baseline subtraction. After excluding regions with peaks, the baseline was fitted to all the remaining points in each spectrum and a polynomial order of eight with the noise tolerance of 1.50 was applied.

Portable set-up. The miniaturised Raman collection optics set-up was machined from aluminium to host the filters and mirrors which were further combined with lens tubes (Thorlabs) to connect the parts together and house the lenses. A 300mW 785nm laser diode unit (PD-LD Inc) was connected to a lens tube *via* an optical fibre. The laser light from the end of the fibre optic was focused to a collimated beam by an aspheric lens (Thorlabs). The collimated beam was reflected downwards by a dichroic mirror (Semrock Inc.) and subsequently, focused to a spot on the SERS substrate by a 20x microscope objective lens (Olympus) at a fixed focus distance of 1.2mm. In the final miniaturised set-up, the reflected scattered light was collected by the microscope objective lens and collimated and subsequently passed through the dichroic mirror until being reflected by a gold mirror and focussed by a lens into the spectrometer, passing through an edge filter to block wavelengths of 785nm and shorter, removing the Rayleigh scattered light and the anti-Stokes signal allowing the Stokes shifted Raman signal through. The focused light then entered the InPhochelle spectrometer where the different frequencies of the Raman light were spread apart and collected onto a CCD detector with the collected spectra analysed by a custom-built MATLAB program.

Calculation of the SERS enhancement factor. For clarity, below we reproduce the principle of the EF calculation from reference [67]. Briefly, SERS enhancement factor was calculated by comparing the intensities of the unenhanced Raman scattering, I_{Raman} peak at 1070cm^{-1} of pure benzenethiol liquid obtained by focusing the laser into a quartz cell and the corresponding SERS signals, I_{SERS} obtained from the SERS substrates. The detection volume of the solution-phase benzenethiol sample, V_f was calculated using the following relation: V_f = (depth of focus) x (focus area) = $(1.4n\lambda/NA2) \times \pi(0.4\lambda/2NA)2$. The surface density of the adsorbed benzenethiol molecules on the structured surface was taken as ρ_s = 3.3molecules/nm^2 and the enhanced area, A was defined as the diffraction limited spot size (= $\pi(0.4\lambda/2NA)2$). The enhancement factor was therefore, calculated using the relation: $EF = [I_{SERS}/(\rho_s A)]/[I_{Raman}/(\rho_v V_f)]$.

Clinical samples. Study participants were recruited through the Surgical Reconstruction and Microbiology Research Centre (SRMRC) at Queen Elizabeth Hospital of Birmingham (UK) as part of the RECOS (Ethics Ref. 11-0429AP28) and the Golden Hour studies (Ethics Ref. 13/WA/0399). Written informed consents were received from participants or valid proxy (family or a professional not directly involved in the study) prior to inclusion in the study. The study was approved by the National Research Ethics Service (Research Ethics Committee reference 13/WA/0399, Integrated Research Application System ID 125988). Both RECOS and

Golden Hour studies comply with the guidelines of the Declaration of Helsinki. The samples were obtained from a standard, widely accepted classification of the TBI severity based on clinical and neurological criteria *i.e.,* the Mayo Classification with initial clinical predictors including age, pupil reactivity, Glasgow Coma Scale (GCS), CT characteristics (Marshall CT classification) and extracranial injury (EC) as well as supported by in-hospital CT and MRI/H^1-MRS scans. Patients were categorised into HV, EC, sTBI and sTBI+EC. EC injury patients had radiographically or clinically-confirmed injuries, no history or signs of head trauma, and no current clinically significant infection, individuals with a history of neurological or psychiatric disorders were excluded. Isolated sTBI patients and sTBI with EC patients were all classified with the severe TBI on the basis of GCS≤8. All patients were gender and age matched to HVs. Patient demographics are shown in Table 1. Blood samples from patients in each category were obtained at different time points post injury: *t*=0 (Golden Hour, at the point-o-care, within less than an hour from injury), *t*=4-12h (8h), t=48h. Peripheral blood samples were taken at the point-of-care study, *i.e.,* Golden Hour patients by pre-hospital clinicians from the West Midlands Medical Emergency Response Intervention Team (MERIT) following initial intravenous access at the scene of injury. Further peripheral blood samples were taken from the same patients during subsequent hospital admission between 4-12h and 48h following the trauma. Once collected, blood samples were left at room temperature for 30 minutes prior to centrifugation at 3000rpm for 10 minutes at 4°C. Serum aliquots were stored at -80°C until analysis. All samples were processed within two hours of venepuncture.

MRI imaging and H^1-MRS spectroscopy. Selected concussed athletes enrolled into the NIHR ReCOS trial without contra-indication to imaging were identified by members of their enhanced-care clinical team and underwent a battery of structural and spectroscopic magnetic resonance (MRS) imaging. This was undertaken on both a Philips Achieva 3.0T and Siemens Magnatom 3.0T magnetic resonance scanners (both utilising 32 channel sensitivity encoding coils) depending on time and practicality constraints surrounding recruitment. A standard structural T1 weighted image was acquired prior to H^1-MRS being undertaken for the purposes of planning. Subsequently, a PRESS (point resolved spectroscopy) sequence (echo time 37ms, relaxation time 2000ms) generated spectra in a 20mm H^1-MRS cubic voxel in right-sided superior frontal white matter (total scanning time 29 minutes). This voxel was consistently selected in each participant, with free hand location to avoid incorporation of the frontal horn of the lateral ventricle of any adjacent grey matter. Movement artefact was minimised by direct observation and real time data review. Echo time was specified (short echo spectrum selected) for improved resolution of lower concentration spectral components.

Spike-and-recovery of the samples. Samples were assessed by adding 50µl of blood sample and 10µl of spike stock NAA solution calculated to yield the intended 0 and 50 pg/ml spike concentrations. Values reported for spiked samples reflected subtraction of the endogenous (no-spike) value. Recoveries for spiked test samples were calculated by comparison to the measured recovery of spiked diluent control. Diluent for the diluent control and preparation of spike stock solutions was the same as the standard diluent. All values represent the average of three replicates. 95.5±3.4% recovery of NAA within the spiked samples was observed. Since the recovery observed for the spike was nearly identical to the recovery obtained for the analyte prepared in standard diluent, the clinical blood samples were considered as valid for the assay system.

Statistical and computational analyses. SERS spectra were analysed for biomarker levels using the software MATLAB® (Natick, MA, version R2015b). MATLAB code can be downloaded from https://gitlab.com/djsmithbham/medtech_projections. All patient data and biomarker spectra were interpolated onto equal-spaced grids using the cubic approximating spline routine 'csaps' (with smoothing parameter set to zero, *i.e.,* no smoothing). The projection of a spectrum $\left(x_j\right)_{j=1}^{n}$ against the kth biomarker $\left(b_j^k\right)_{j=1}^{n}$ was computed *via* dot products, *i.e.,* $P^k\left(x_j\right) = \frac{\sum_{j=1}^{n} x_j b_j^k}{\sum_{j=1}^{n}\left(b_j^k\right)^2}$. Projections for control and patient spectra were compared for each biomarker in turn using the Wilcoxon rank sum/Mann-Whitney U test. Spearman rank correlation coefficients were calculated with the function 'coef' in Mathworks software MATLAB. Correlation analysis between each set of projections was carried out with the MATLAB® routine 'corrcoef'. Logistic regression was performed with the MATLAB® routine 'fitglm' sequentially on models consisting of each possible combination of 1, 2 and all 3 projections P^k as predictors of HV or GH group. Spearman rank correlation coefficients were calculated with the function 'coef' in Mathworks software Matlab. Principal components analysis was performed with OriginPro 9.0 and MATLAB (The MathWorks, Inc.) with advanced chemometric software and PLS Toolbox

8.2 (Eigenvector Inc.). The data of the mild TBI cohort was checked for normal distribution and transformed to perform parametric tests. Comparisons across groups at each time and within groups over time were performed by the analysis of variance and Tukey's post hoc test on transformed data. *p* value <0.05 was considered significant. All analyses were carried on SPSS v.22 (IBM).

Classification matrices. To acquire a classification of the SERS data, a feature selection of an optimal subset of relevant features was used to establish the important peaks and their correlations and thus, it contains the least number of features, discarding the unimportant ones.[42] Firstly, by calculating the highest *a posteriori* probability (maximum *a posterior* method), according to the classification rule of: "select the class, wi, in the maximum a posterior classifier that maximised the posterior probability, $P(x|wi)$, and if $P(x|wi) \geq P(x|wi+1)$", then primary significant peaks yielding the most discriminality from the pre-processed spectrum were chosen as the feature candidates for classification with the most discriminating peak selected as a reference feature at 1420cm^{-1}. Consequently, the ratio of intensity of all primary peaks yields the extended feature set. This was followed by computing the correlation coefficients between the reference peak and each chosen peak and finally, the highly correlated features *i.e.,* with correlation coefficients >0.35, had been discarded. Since both the ratio of peaks intensities as well as the intensity itself of various peaks can be used for SERS classification, the feature set included the optimal possible combinations of primary peaks and ratios. Table in the Supplementary Figure S7 summarises the classification rates of the primary peaks and the correlation coefficients. Ranking the classification performance and examining the features of the top ten percent of the cases, the most frequently appearing features included, intensity and the ratio of the peaks at 1420cm^{-1} and 1517cm^{-1} and 682, 717, 930, 1010, 1168cm^{-1}. The multi-layer perception classifier with the selected features enabled a consideration of all possible variables within the SERS spectra set and of their significance for the discrimination between classes. The models' unit operation equation is given by the activation function, f() and the input to the unit, net_k: $\mathbf{o}_k = f(net_k)$ using the back-propagation algorithm, these were trained to output (+1) for HVs group and (-1) for sTBI group. These variables were taken into a consideration due the reduction of the original SERS spectra to subsets of wave-numbers, simplifying the spectral dataset for the possible identification of meaningful information. The Raman bands that yielded the best results for internal cross validation were identified from the most informative spectral regions. These regions and bands represent spectroscopic markers for the datasets in the study.

ROC curves and box plots. ROC curves were generated from patient profiling data for different cut-off points using non-parametric Mann-Whitney U and Kruskal Wallis tests, run using SPSS statistics software.[47] Each point in the ROC curve represented a sensitivity/specificity pair corresponding to a particular decision threshold and the diagnostic values of sensitivity, specificity, and accuracy were calculated using standard equations. A test with perfect discrimination (no overlap in the two distributions) had an ROC curve that passed through the upper left corner (100% sensitivity, 100% specificity). Therefore the closer the ROC curve was to the upper left corner, the higher was the overall accuracy of the test. Box plots were generated using the Vertex42 LLC software where each of the series is an x-y chart used to represent the quartiles and allows the data to include negative values. The median is represented with an "x" marker and horizontal markers are used for Q_1 and Q_3 without requiring shifting of the data. The mean levels of TBI patients' group comparison to healthy volunteers control group were performed using two-sided normal-based 95% CIs *t*-test. Classification sensitivity, accuracy and specificity were determined on the basis of sTBI detection results: Sensitivity=(TP)/(TP+FN), Specificity=(TN)/(TN+FP) and the Accuracy= (TP+TN)/(TP+TN+FN+FP) with TP being 'true positive', TN 'true negative', FP and FN 'false positive' and 'false negative', accordingly.

Microfluidic chip fabrication. A master mold for the microfluidic chip was fabricated using photolithography. Initially, a copper substrate was polished to a fine finish and subsequently, spin-coated with a 2μm layer of AZ positive photoresist (1514H). Using a chrome mask, the photoresist was exposed under UV light at a wavelength of 365nm and then developed using AZ developer (Supplementary Fig. S20, a-b). Subsequently, the copper master was etched in a ferric chloride bath for 2 minutes, yielding an etched depth of 10μm and then further etched by a focused ion-beam milling microscope (FEI Helios) at 30kV (gallium ions), generating fine filter combs between the main capillary channel and the collection reservoirs (Supplementary Fig. S20, c). Small pieces of silicon wafer were glued over the collection regions areas to enable bigger cavities and an ease of cutting these out once the chip is moulded. Thereafter, to cast the microfluidic chip, the etched master was covered with polydimethylsiloxane (PDMS). Following the curing at 125 °C for 20 minutes, the holes for

blood input and for the collection regions as well as the ending of the capillary collection reservoir were carefully stencilled. The PDMS was then smoothly peeled off the master. Subsequently, microscope glass slides were cleaned for 30 minutes in Piranha solution (H_2SO_4:H_2O_2, 3:1) at 80°C, rinsed with distilled water and finally dried under a nitrogen stream. The PDMS copy and a glass integrated with the SERS detection substrate were subsequently treated in plasma cleaner for 1.20 minutes. Finally, the PDMS replica was carefully placed on top of the glass slides aligning the holes for the collection regions over the SERS active area, allowing the PDMS to bond to the slide.

Optical microscopy. Pattern formation in thin polymer films was qualitatively analysed using a bright-field reflection microscopy (Olympus Optical Microscopes GX61, GX2 and BX40). The reflection of white light from the sample enabled resolving the submicron scale features. The evolving patterns were also observed by the *in-situ* monitoring of the electrohydrodynamic pattern formation and replication in thin films employing a digital camera and imaging software (Carl Zeiss VisioCam, AxioVision).

Atomic force microscopy. NanoScope IV Multimode and Dimension 3100 (Digital Instruments, Santa Barbara, CA) atomic force microscope was used to thoroughly characterise the surfaces' topography. The AFM measurements were performed using tapping mode via an intermittent contact of the tip with the sample, in ambient conditions. NSG 20 cantilevers with a resonance frequency of 260 kHz and a stiffness of 28Nm^{-1} were used. Height and phase images were analysed with the Nanoscope software (Digital Instruments, v. v140r1). The AFM measurements were uses to acquire important parameters including, the film thickness h, the inter-electrode spacing d, the characteristic wavelength λ and the aspect ratio, $f=h/d$, of the generated structures.

Scanning electron microscopy. Samples for SEM imaging were prepared by placing a post-experiment, disassembled substrate with the generated patterns on an inclined or cross-sectional holder to enable the imaging of the top and cross-sectional views. Scanning electron micrographs were acquired using a thermally assisted Field Emission Scanning Electron Microscope (FESEM, LEO VP 1530 and FEI Magellan and Helios) with a lateral resolution of 2-5nm. A LEO ULTRA 55 SEM instrument including a Schottky emitter (ZrO/W cathode) was also used for imaging the samples with a typical acceleration voltage of 2-5kV.

Reporting Summary. Further information on experimental design is available in the Nature Research Reporting Summary linked to this article.

Data Availability

The main data supporting the results in this study are available within the paper and the Supplementary Information. The study was approved by the North Wales Ethics Committee (REC reference 13/WA/0399, Protocol number RG_13-164, IRAS project ID 125988). The raw datasets generated and analysed in this study and the source data for the figures are available in *figshare* with the identifier(s) [https://doi.org/10.6084/m9.figshare.11302364.v2 (2019)] [107].

Code Availability

MATLAB code can be downloaded from https://gitlab.com/djsmithbham/medtech_projections.

References

1. Dash, P.K., Zhao, J., Hergenroeder, G. & Moore, A.N. Biomarkers for the Diagnosis, Prognosis, and Evaluation of Treatment Efficacy for Traumatic Brain Injury. *Neurotherapeutics* **7**, 100-114 (2010).
2. Neurotrauma *World Health Organisation Report, Geneva* (2016).
3. Robertson, C. & Rangel-Castilla, L. in Critical Care Management of Traumatic Brain Injury (2015).
4. DeKosky , S.T., Ikonomovic , M.D. & Gandy , S. Traumatic Brain Injury - Football, Warfare, and Long-Term Effects. *New England Journal of Medicine* **363**, 1293-1296 (2010).
5. Carney, N. et al. Guidelines for the Management of Severe Traumatic Brain Injury. *Brain Trauma Foundation*, 1-244 (2016).
6. Aquino, C., Woolen, S. & Steenburg, S.D. Magnetic resonance imaging of traumatic brain injury: a pictorial review. *Emergency Radiology* **22**, 65-78 (2015).
7. Di Costanzo, A. et al. High-field proton MRS of human brain. *European Journal of Radiology* **48**, 146-153 (2003).

8. Xiong, K.-l., Zhu, Y.-s. & Zhang, W.-g. Diffusion tensor imaging and magnetic resonance spectroscopy in traumatic brain injury: a review of recent literature. *Brain Imaging and Behavior* **8**, 487-496 (2014).
9. Croall, I., Smith, F.E. & Blamire, A.M. Magnetic Resonance Spectroscopy for Traumatic Brain Injury. *Topics in Magnetic Resonance Imaging* **24**, 267-274 (2015).
10. L., D.E. et al. Magnetic resonance spectroscopy of fiber tracts in children with traumatic brain injury: A combined MRS – Diffusion MRI study. *Human Brain Mapping* **39,** 3759-1768 (2018).
11. Haddad, H.S. & Arabi, M.Y. Critical care management of severe traumatic brain injury in adults. *Scandinavian Journal of Trauma, Resuscitation and Emergency Medicine* **20**, 1-15 (2012).
12. Ling, G.S.F. & Marshall, S.A. Management of traumatic brain injury in the intensive care unit. *Neurologic Clinics* **26**, 409-426 (2008).
13. Dinsmore, J. Traumatic brain injury: an evidence-based review of management. *Continuing Education in Anaesthesia Critical Care & Pain* **13**, 189-195 (2013).
14. Zetterberg, H., Smith, D.H. & Blennow, K. Biomarkers of mild traumatic brain injury in cerebrospinal fluid and blood. *Nature reviews. Neurology* **9**, 201-210 (2013).
15. Skolnick, B.E. et al. A clinical trial of progesterone for severe traumatic brain injury. *New England Journal of Medicine* **371**, 2467-2476 (2014).
16. Teasdale, G. & Jennett, B. Assessment of coma and impaired consciousness: a practical scale. *The Lancet* **304**, 81-84 (1974).
17. Teasdale, G., Murray, G., Parker, L. & Jennett, B. 13-16 (Springer Vienna, Vienna; 1979).
18. Azouvi, P., Arnould, A., Dromer, E. & Vallat-Azouvi, C. Neuropsychology of traumatic brain injury: An expert overview. *Revue Neurologique* **173**, 461-472 (2017).
19. Dadas, A., Washington, J., Diaz-Arrastia, R. & Janigro, D. Biomarkers in traumatic brain injury (TBI): a review. *Neuropsychiatric disease and treatment* **14**, 2989-3000 (2018).
20. Maas, A.I.R. et al. Traumatic brain injury: integrated approaches to improve prevention, clinical care, and research. *The Lancet Neurology* **16**, 987-1048 (2017).
21. Moffett, J., Arun, P., Ariyannur, P. & Namboodiri, A. N-Acetylaspartate reductions in brain injury: impact on post-injury neuroenergetics, lipid synthesis, and protein acetylation. *Frontiers in Neuroenergetics* **5** (2013).
22. O'Connell, B. et al. Use of Blood Biomarkers in the Assessment of Sports-Related Concussion—A Systematic Review in the Context of Their Biological Significance. *Clinical Journal of Sport Medicine* **28**, 561-571 (2018).
23. Rubenstein, R., Chang, B., Yue, J.K. & et al. Comparing plasma phospho tau, total tau, and phospho tau–total tau ratio as acute and chronic traumatic brain injury biomarkers. *JAMA Neurology* **74**, 1063-1072 (2017).
24. Vella, M.A., Crandall, M.L. & Patel, M.B. Acute Management of Traumatic Brain Injury. *Surgical Clinics of North America* **97**, 1015-1030 (2017).
25. Bazarian, J.J. et al. Serum GFAP and UCH-L1 for prediction of absence of intracranial injuries on head CT (ALERT-TBI): a multicentre observational study. *The Lancet Neurology* **17**, 782-789 (2018).
26. Stocchetti, N. et al. Severe traumatic brain injury: targeted management in the intensive care unit. *The Lancet Neurology* **16**, 452-464 (2017).
27. Mapstone, M. et al. Plasma phospholipids identify antecedent memory impairment in older adults. *Nature Medicine* **20**, 415 (2014).
28. Sharma, R. & Laskowitz, D.T. Biomarkers in Traumatic Brain Injury. *Current Neurology and Neuroscience Reports* **12**, 560-569 (2012).
29. Papa, L. et al. Elevated Levels of Serum Glial Fibrillary Acidic Protein Breakdown Products in Mild and Moderate Traumatic Brain Injury Are Associated With Intracranial Lesions and Neurosurgical Intervention. *Annals of Emergency Medicine* **59**, 471-483 (2012).
30. Sen, J. et al. Extracellular fluid S100B in the injured brain: a future surrogate marker of acute brain injury? *Acta Neurochirurgica* **147**, 897-900 (2005).
31. Thelin, E.P. et al. Utility of neuron-specific enolase in traumatic brain injury; relations to S100B levels, outcome, and extracranial injury severity. *Critical Care* **20**, 285 (2016).
32. B. Patel, T. & B. Clark, J. Synthesis of N-acetyl-L-aspartate by rat brain mitochondria and its involvement in mitochondrial/cytosolic carbon transport. *Bicohemical Journal* **184**, 539-546 (1980).
33. J., S.R. et al. Extracellular N-Acetylaspartate in Human Traumatic Brain Injury. *Journal of Neurotrauma* **33**, 319-329 (2016).
34. Belli, A. et al. Extracellular N-acetylaspartate depletion in traumatic brain injury. *Journal of Neurochemistry* **96**, 861-869 (2006).
35. Vespa, P. et al. Metabolic Crisis without Brain Ischemia is Common after Traumatic Brain Injury: A Combined Microdialysis and Positron Emission Tomography Study. *Journal of Cerebral Blood Flow & Metabolism* **25**, 763-774 (2005).
36. Nadler, J.V. & Cooper, J.R. N-acetyl-L-aspartic acid content of human neural tumours and bovine perioheralnervous tissues. *Journal of Neurochemistry* **19**, 313-319 (1972).

37. Benarroch, E.E. N-Acetylaspartate and N-acetylaspartylglutamate. *Neurobiology and clinical significance* **70**, 1353-1357 (2008).
38. Sinson, G. et al. Magnetization Transfer Imaging and Proton MR Spectroscopy in the Evaluation of Axonal Injury: Correlation with Clinical Outcome after Traumatic Brain Injury. *American Journal of Neuroradiology* **22**, 143-151 (2001).
39. Blamire, A.M., Rajagopalan, B., Garnett, M.R., Styles, P. & Cadoux-Hudson, T.A.D. Evidence for cellular damage in normal-appearing white matter correlates with injury severity in patients following traumatic brain injury: A magnetic resonance spectroscopy study. *Brain* **123**, 1403-1409 (2000).
40. Kahraman, M., Mullen Emma, R., Korkmaz, A. & Wachsmann-Hogiu, S. *Nanophotonics*, **6**, 831 (2017).
41. Weigao, X., Nannan, M. & Jin, Z. Graphene: A platform for surface-enhanced Raman spectroscopy. *Small* **9**, 1206-1224 (2013).
42. Huang, S. et al. Molecular selectivity of graphene-enhanced Raman scattering. *Nano Letters* **15**, 2892-2901 (2015).
43. Moore, T. et al. *In Vitro* and *In Vivo* SERS biosensing for disease diagnosis. *Biosensors* **8**, 46 (2018).
44. Wang, R. et al. in Frontiers and Advances in Molecular Spectroscopy. (ed. J. Laane) 307-326 (Elsevier, 2018).
45. Han, X.X., Ozaki, Y. & Zhao, B. Label-free detection in biological applications of surface-enhanced Raman scattering. *TrAC Trends in Analytical Chemistry* **38**, 67-78 (2012).
46. Han, X.X., Zhao, B. & Ozaki, Y. Surface-enhanced Raman scattering for protein detection. *Analytical and Bioanalytical Chemistry* **394**, 1719-1727 (2009).
47. Wang, Y. et al. Quantitative molecular phenotyping with topically applied SERS nanoparticles for intraoperative guidance of breast cancer lumpectomy. *Scientific Reports* **6**, 21242 (2016).
48. Wang, Y.W. et al. Rapid ratiometric biomarker detection with topically applied SERS nanoparticles. *Technology* **2**, 118-132 (2014).
49. McQueenie, R. et al. Detection of inflammation in vivo by surface-enhanced Raman scattering provides higher sensitivity than conventional fluorescence imaging. *Analytical Chemistry* **84**, 5968-5975 (2012).
50. Barnes, W.L., Dereux, A. & Ebbesen, T.W. Surface plasmon subwavelength optics. *Nature* **424**, 824-830 (2003).
51. Kneipp, K. et al. Single molecule detection using surface-enhanced raman scattering (SERS). *Physical Review Letters* **78**, 1667-1670 (1997).
52. Nie, S. & Emory, S.R. Probing single molecules and single nanoparticles by surface-enhanced Raman scattering. *Science* **275**, 1102-1106 (1997).
53. Ozbay, E. Plasmonics: merging photonics and electronics at nanoscale dimensions. *Science* **311**, 189-193 (2006).
54. Dinish, U.S., Balasundaram, G., Chang, Y.T. & Olivo, M. Sensitive multiplex detection of serological liver cancer biomarkers using SERS-active photonic crystal fiber probe. *Journal of Biophotonics* **7**, 956-965 (2014).
55. Dinish, U.S., Balasundaram, G., Chang, Y.-T. & Olivo, M. Actively targeted in vivo multiplex detection of intrinsic cancer biomarkers using biocompatible SERS nanotags. *Scientific Reports* **4**, 4075 (2014).
56. Socrates, G., Edn. 3rd ed. (ed. G. Socrates) (Wiley, Chichester; 2001).
57. O. Durucan, L.M., M. Stenbæk Schmidt, R. Burger, T. Rindzevicius and A. Boisen detection of bacterial metabolites through dynamic acquisition from surface enhanced raman spectroscopy substrates integtrated in a centrifugal microfluidic platform *19th International Conference on Miniaturized Systems for Chemistry and Life Sciences* 1831-1833 (2015).
58. Hoonejani, M.R., Pallaoro, A., Braun, G.B., Moskovits, M. & Meinhart, C.D. Quantitative multiplexed simulated-cell identification by SERS in microfluidic devices. *Nanoscale* **7**, 16834-16840 (2015).
59. Chen, G. et al. A highly sensitive microfluidics system for multiplexed surface-enhanced Raman scattering (SERS) detection based on Ag nanodot arrays. *RSC Advances* **4**, 54434-54440 (2014).
60. Jahn, I.J. et al. Surface-enhanced Raman spectroscopy and microfluidic platforms: challenges, solutions and potential applications. *Analyst* **142**, 1022-1047 (2017).
61. Chen, L. & Choo, J. Recent advances in surface-enhanced Raman scattering detection technology for microfluidic chips. *Electrophoresis* **29**, 1815-1828 (2008).
62. Gauglitz, G. & Moore, D.S. Handbook of spectroscopy. (2014).
63. Pennathur, S. & Fygenson, D. Improving fluorescence detection in lab on chip devices. *Lab on a Chip* **8**, 649-652 (2008).
64. Kho, K. et al. Polymer-based microfluidics with surface-enhanced Raman-spectroscopy-active periodic metal nanostructures for biofluid analysis. *Journal of Biomedical Optics* **13**, 054026 (2008).
65. Granger, J.H., Schlotter, N.E., Crawford, A.C. & Porter, M.D. Prospects for point-of-care pathogen diagnostics using surface-enhanced Raman scattering (SERS). *Chemical Society Reviews* **45**, 3865-3882 (2016).
66. Goldberg-Oppenheimer, P., Mahajan, S. & Steiner, U. Hierarchical Electrohydrodynamic Structures for Surface-Enhanced Raman Scattering. *Advanced Materials* **24**, OP175-OP180 (2012).

67. Mahajan, S., Hutter, T., Steiner, U. & Goldberg Oppenheimer, P. Tunable Microstructured Surface-Enhanced Raman Scattering Substrates *via* Electrohydrodynamic Lithography, Vol. 4. (2013).
68. Banbury, C., Rickard, J.J.S., Mahajan, S. & Goldberg Oppenheimer, P. Tuneable Metamaterial-like Platforms for Surface-Enhanced Raman Scattering *via* Three-Dimensional Block Co-polymer-Based Nanoarchitectures. *ACS Applied Materials & Interfaces* **11**, 14437-14444 (2019).
69. Goldberg-Oppenheimer, P. et al. Optimized vertical carbon nanotube forests for multiplex surface-enhanced raman scattering detection. *The Journal of Physical Chemistry Letters* **3**, 3486-3492 (2012).
70. Piorek, B.D. et al. Free-surface microfluidic control of surface-enhanced Raman spectroscopy for the optimized detection of airborne molecules. *Proceedings of the National Academy of Sciences* **104**, 18898-18901 (2007).
71. Qian, X., Zhou, X. & Nie, S. Surface-Enhanced Raman Nanoparticle Beacons Based on Bioconjugated Gold Nanocrystals and Long Range Plasmonic Coupling. *J. Am. Chem. Soc.* **130**, 14934–14935 (2008).
72. Ackermann, L., Althammer, A. & Born, R. Catalytic Arylation Reactions by CH Bond Activation with Aryl Tosylates. *Angewandte Chemie International Edition* **45**, 2619-2622 (2006).
73. Lim, C., Hong, J., Chung, B.G., deMello, A.J. & Choo, J. Optofluidic platforms based on surface-enhanced Raman scattering. *Analyst* **135**, 837-844 (2010).
74. Jie Chang, X.Z., and Amin Zhang Application of Graphene in Surface-Enhanced Raman Spectroscopy. *Nano Biomedicine and Engineering* **9**, 49-56. (2017).
75. Goldberg Oppenheimer, P., Rickard, J.J.S., Di-Pietro, V. & Belli, A., Vol. 1701182.6 (2017).
76. E.R., D. & B, R. Magnetic resonance spectroscopy diagnosis of neurological diseases. 1st Edition. (Marcel Dekker, Inc, New York; 1999).
77. Tshibanda, J.-F.L., Demertzi, A. & Soddu, A. in Coma and Disorders of Consciousness. (eds. C. Schnakers & S. Laureys) 45-54 (Springer, London; 2012).
78. Coon, A.L. et al. Correlation of cerebral metabolites with functional outcome in experimental primate stroke using in vivo H-magnetic resonance spectroscopy. *American Journal of Neuroradiology* **27**, 1053-1058 (2006).
79. Schuff, N. et al. Selective reduction of N-acetylaspartate in medial temporal and parietal lobes in AD. *Neurology* **58**, 928-935 (2002).
80. Shannon, R.J. et al. Extracellular N-acetylaspartate in human traumatic brain injury. *Journal of Neurotrauma*, 319–329 (2016).
81. Hoshino, H. & Kubota, M. Canavan disease: Clinical features and recent advances in research. *Pediatrics International* **56**, 477-483 (2014).
82. Di Pietro, V. et al. New T530C mutation in the aspartoacylase gene caused Canavan disease with no correlation between severity and N-acetylaspartate excretion. *Clinical Biochemistry* **46**, 1902-1904 (2013).
83. Dadas, A., Washington, J., Marchi, N. & Janigro, D. Improving the clinical management of traumatic brain injury through the pharmacokinetic modeling of peripheral blood biomarkers. *Fluids and Barriers of the CNS* **13**, 21 (2016).
84. Lin, S.-N., Slopis, J.M., Butler, I.J. & Caprioli, R.M. In vivo microdialysis and gas chromatography/mass spectrometry for studies on release of N-acetylaspartlyglutamate and N-acetylaspartate in rat brain hypothalamus. *Journal of Neuroscience Methods* **62**, 199-205 (1995).
85. Rigotti, D.J., Inglese, M. & Gonen, O. Whole-Brain N-Acetylaspartate as a surrogate marker of neuronal damage in diffuse neurologic disorders. *American Journal of Neuroradiology* **28**, 1843-1849 (2007).
86. Park, A., Baek, S.-J., Shen, A. & Hu, J. Detection of Alzheimer's disease by Raman spectra of rat's platelet with a simple feature selection. *Chemometrics and Intelligent Laboratory Systems* **121**, 52-56 (2013).
87. Shen, A. et al. In vivo study on the protection of indole-3-carbinol (I3C) against the mouse acute alcoholic liver injury by micro-Raman spectroscopy. **40**, 550-555 (2009).
88. R.O. Duda, P.E. Hart, and D.G. Stork, Pattern Classification, New York: John Wiley & Sons, 2001, pp. xx + 654, ISBN: 0-471-05669-3. *J. Classif.* **24**, 305-307 (2007).
89. Aiguo, S. et al. In vivo study on the protection of indole-3-carbinol (I3C) against the mouse acute alcoholic liver injury by micro-Raman spectroscopy. *Journal of Raman Spectroscopy* **40**, 550-555 (2009).
90. Vagnozzi, R. et al. Temporal window of metabolic brain vulnerability to concussions: Mitochondrial-related impairment - Part I, Vol. 61. (2007).
91. Vagnozzi, R. et al. Temporal window of metabolic brain vulnerability to concussion: A pilot 1H-magnetic resonance spectroscopic study in concussed athletes - Part III, Vol. 62. (2008).
92. Veeramuthu, V. et al. Neurometabolites alteration in the acute phase of mild traumatic brain injury (mTBI). *Academic Radiology*.
93. Brown, M. et al. Magnetic resonance spectroscopy abnormalities in traumatic brain injury: A meta-analysis. *Journal of Neuroradiology* **45**, 123-129 (2018).

94. Andrew, G., L., I.G. & Peter, S. A systematic review of proton magnetic resonance spectroscopy findings in sport-related concussion. *Journal of Neurotrauma* **31**, 1-18 (2014).
95. Vagnozzi, R. et al. Assessment of metabolic brain damage and recovery following mild traumatic brain injury: a multicentre, proton magnetic resonance spectroscopic study in concussed patients. *Brain* **133**, 3232-3242 (2010).
96. Stovell, M.G. et al. Assessing metabolism and injury in acute human traumatic brain injury with magnetic resonance spectroscopy: current and future applications. *Frontiers in Neurology* **8**, 426 (2017).
97. Dimov, I.K. et al. Stand-alone self-powered integrated microfluidic blood analysis system (SIMBAS). *Lab on a Chip* **11**, 845-850 (2011).
98. Szydzik, C., Khoshmanesh, K., Mitchell, A. & Karnutsch, C. Microfluidic platform for separation and extraction of plasma from whole blood using dielectrophoresis. *Biomicrofluidics* **9**, 064120 (2015).
99. Srivastava, S.K. et al. Highly sensitive and specific detection of *E. coli* by a SERS nanobiosensor chip utilizing metallic nanosculptured thin films. *Analyst* **140**, 3201-3209 (2015).
100. Lin, D. et al. Label-free blood plasma test based on surface-enhanced Raman scattering for tumor stages detection in nasopharyngeal cancer. *Scientific Reports* **4**, 4751 (2014).
101. Yang, S., Dai, X., Stogin, B.B. & Wong, T.-S. Ultrasensitive surface-enhanced Raman scattering detection in common fluids. *Proceedings of the National Academy of Sciences* **113**, 268-273 (2016).
102. Muniz-Miranda, M. et al. Nanostructured films of metal particles obtained by laser ablation. *Thin Solid Films* **543**, 118-121 (2013).
103. Premasiri, W.R., Lee, J.C. & Ziegler, L.D. Surface-enhanced Raman scattering of whole human blood, blood plasma, and red blood cells: cellular processes and bioanalytical sensing. *The Journal of Physical Chemistry B* **116**, 9376-9386 (2012).
104. Tran Cao, D. et al. Trace detection of herbicides by SERS technique, using SERS-active substrates fabricated from different silver nanostructures deposited on silicon. *Advances in Natural Sciences: Nanoscience and Nanotechnology* **6**, 035012 (2015).
105. U. S, D. et al. Highly sensitive SERS detection of cancer proteins in low sample volume using hollow core photonic crystal fiber. *Biosensors and Bioelectronics* **33**, 293-298 (2012).
106. Juncker, D. et al. Autonomous microfluidic capillary system. *Analytical Chemistry* **74**, 6139-6144 (2002).
107. Rickard, J.J.S.R. *et* al. Dataset for the 'Rapid optofluidic detection of biomarkers for traumatic brain injury *via* surface-enhanced Raman spectroscopy'. *figshare*. Dataset. https://doi.org/10.6084/m9.figshare.11302364.v2 (2019).

Acknowledgements

We acknowledge funding from the Wellcome Trust (174ISSFPP), the Royal Academy of Engineering (RF1415\14\28) and the National Institute for Health Research (NIHR, DTAARGCQ19497). P.G.O. is a Royal Academy of Engineering Research (RAEng) Fellowship holder. The authors also thank M.J. Rowney and F.M. Colacino for helpful discussion about the technology and insights into classification analyses. Components of the developed device were fabricated using the facilities at the Cavendish Laboratories at the Department of Physics and the Nanoscience Centre for Fabrication (NCF) at the University of Cambridge.

Author Contributions

P.G.O. and A.B. conceptualised the study and with J.J.S.R. designed the project and the experiments. J.J.S.R. fabricated the SERS substrates and the optofluidic devices and with P.G.O. carried out the imaging. J.J.S.R. performed material and device characterization, D.J.S. performed the computational and statistical data analysis and classification and D.J.D. carried out the MRI, the H^1-MRS data collection and the corresponding data analysis. V.D.P. and D.J.D. collected and coordinated the clinical samples and with A.B., established the ethics for this study. J.J.S.R., V.D.P. and P.G.O. prepared the schematics and images and J.J.S.R. with P.G.O. carried out devices engineering and optimisation. J.J.S.R. and V.D.P. performed the tests on the clinical samples with the corresponding statistical analyses and with P.G.O. analysed the data. All authors carried out the data analysis on the corresponding parts of the study. J.J.S.R., A.B. and P.G.O. wrote the manuscript. All authors reviewed and commented on the manuscript.

Competing interests

Authors declare no competing interests.

Additional information

Supplementary information is available for this paper at https://doi.org/10.1038/s41551-01X-XXXX-X.

Figure captions

Fig. 1 | Optimised biodiagnostic platforms. a, The current 'gold-standard' for TBI using (i) MRI for brain imaging (**top left inset**) and the corresponding *in-vivo* H^1-MRS shows lower NAA levels (**bottom left inset**) in specific cortical brain areas of patients with sTBI. For fabricating the reproducible electrohydrodynamic platforms (ii) a micro-capacitor like lithographic device is assembled using a thin nanofilm on a Si wafer as a lower electrode. Facing it, a top electrode is mounted to generate a high homogeneous electric field while leaving a thin nano-gap. The 'wedge-geometry' of the micro-capacitor yields electrohydrodynamically generated pillars with a distribution of aspect ratios. With an optimal aspect ratio for SERS platforms established at 0.8, (iii) reproducible electrohydrodynamic substrates are fabricated *via* (iv) designing and fabricating a lithographically structured top electrode with set inter-electrode gap and diameter of the protruding structures, enabling production of highly-reproducible pillars in a controlled manner. All optical images (n=10) are as-acquired and the colours arise from the thickness and height distribution of the polymer on the underlying silicon substrate. **b,** Corresponding atomic force microscopy (AFM) images show the (i) lateral distribution of the EHD pillars (100x100μm^2, each gridline 25μm), (ii) reproducible electrohydrodynamically generated pillars under a homogeneous electric field and (iii) optimsied pillars fabricated *via* a dedicated set-up for highly-reproducible SERS substrates (50x50μm^2, each gridline 10μm). (iv) Scanning electron microscopy (n=5) image of gold-coated structures confirms smooth and conformal coverage of generated structures. **c,** A dedicated rig is engineered to fabricate the electrohydrodynamically generated substrates comprising a copper block on top of which is mounted a thin beryllium copper spring clamp to hold the bottom substrate in place and connect the bottom substrate to ground. The micrometre allows 'course' micro-adjustment of the gap between the top and bottom electrode within a few microns. The top half of the rig is made of glass which clamps around the rectangular glass pillar using a beryllium copper spring clamp. Protruding from one end of the glass spars is a piezo actuator and finally, an additional block of glass and stuck to that block is another thin beryllium copper spring clamp that clamps the top substrate and allows a connection to the positive power supply. The piezo actuator allows the finest (nano) adjustments of the gap between the top and bottom substrate. **d,** Reproducible spectra of benzenethiol (n=17) on electrohydrodynamically generated substrates across different areas reveal consistent signal and substrate regularity. Insets: (i) A photograph of the gold coated platform with an active area at the bottom right corner. (ii) A representative SERS map overlaid on top of the corresponding optical image reveals that the SERS signal (red) comes exclusively from the RED pillars. No SERS signal is observed from the flat gold or in between the pillars. (iii) FTDT simulation shows the enhanced electromagnetic fields tightly confined on top of periodic pillar surface, maximizing the detection sensitivity.

Fig. 2 | Analytical and computational quantification of TBI indicative biomarkers with optofluidic SERS device. a, Histogram of the measured electromagnetic enhancement factors of the reproducible electrohydrodynamically (RED) generated substrates (n=17) shows a narrow distribution with an average enhancement on the scale of $8x10^9$. Inset: PCA score plots of PC1 and PC2 show the relationship between the multiplex spectra of the three single biomarkers. The blue cluster is the NAA spectra (n=23), the purple cluster represents the S100B (n=18) and the red is the GFAP (n=13). Underlying calculations are in Supplementary Figure S7. Error bars denote standard deviation (s.d.) **b,** The assay was performed for each biomarker using the specified concentration range yielding calibration curves of SERS spectra acquired with an excitation laser of 785nm each point representing an average of five measurements (n=5) of each concentration ± s.d. used to calculate the LoD and LoQ using peak height of 1420cm^{-1} for the NAA, 1070cm^{-1} for S100B and 1150cm^{-1} for the GFAP. Inset: representative NAA levels as function of SERS intensity for the dilution series and the calculated LoD values for each biomarker (**inset table**). **c,** Wilcoxon rank sum/Mann-Whitney U test projections on the NAA biomarker reveal a significant difference between the sTBI and HV groups. Red line represents the median, top and bottom edges of box are the upper and lower quartiles, whiskers extend to upper and lower quartiles plus and minus 1.5x interquartile range, respectively crosses

indicate values outlying the whiskers. The central mark is the median, the edges of the box are the 25th and 75th percentiles, the whiskers extend to the most extreme data points the algorithm considers to be not outliers (outliers are $q_3 + 1.5 \times (q_3-q_1)$ or less than $q_1-1.5\times(q_3-q_1)$ where q_1 is 25th percentile and q_3 is 75th percentile). Wilcoxon rank sum, two-tailed, no adjustment for multiple comparisons (n=40), p=9.3451e-03, z=-2.5992e+00. **d,** Classification matrices of the feature selection of subset of relevant features, used to establish the important peaks and their correlations reveals decision boundaries of multi-layer perception with distribution of the selected peaks with clear separation at each subset between the sTBI and the HV patients. Inset: The NAA molecular structure and the major assignments of major SERS peaks of NAA on RED substrate. σ, stretching vibration, δ, bending vibration, δ_s-symmetric bending vibration, ρ-rocking, in-plane bending, γ-wagging, ν-breathing, τ-twisting; Raman intensity: *s*-strong, *m*-medium, *w*-weak. **e,** Average SERS spectrum (n=5) of (i) HVs (bottom panel) excited at 785nm are compared to the SERS spectrum of (ii) sTBI only and (iii) sTBI+EC and to the finger print spectrum of the (iv) NAA (upper panel) with the representative significant peaks highlighted with vertical (i) grey, (ii) blue, (iii) red and (iv) dotted lines, accordingly, highlighting the correspondence or the absence of the NAA peaks with some vibrational frequencies of the bands being unchanged in SERS spectra whereas several are red shifted or not evident in the HVs spectrum. Inset: Barcode derived from SERS spectra shown in (**e**) for sTBI diagnostics.

Fig. 3 | Temporal profiling of the NAA blood plasma levels post TBI. **a,** SERS spectra show decreasing levels of the NAA as a function of time from t=0 through t=8h (4-12h) and to t=48h following sTBI. **Inset**: CT scans of the positive sTBI (left) with typical lesions indicated by arrows and the negative sTBI (right) for clinical diagnoses. **b,** Box and whisker plots represent the minima, maxima, interquartile ranges, whiskers and the median in plasma levels of the NAA tested within t=0 to t=48h in patients with sTBI ($n_{patients}$=11, $n_{samples}$=37), sTBI+EC ($n_{patients}$ =24, $n_{samples}$=75) *versus* HV ($n_{patients}$ =23, $n_{samples}$=82) and EC ($n_{patients}$=8, $n_{samples}$=27) controls. In all three groups, relative to the HV, the NAA levels have increased at t=0 and subsequently, decreased incrementally with time. (**c-e**). ROC plots representing the Sensitivity *versus* 1-Specificity derived from three time points following the sTBI applied to determine the success for classifying the sTBI, EC only and HV groups at (**c**) t=0 (p=0.000) (**d**) t=8h (p=0.002) and (**e**) t=48h (p=0.003); two-sided test with no multiple comparisons. The AUC indicates that the change in the NAA levels following the sTBI is a valuable marker to discriminate sTBI from the EC with the NAA showing an excellent performance with AUC=0.99 at t=0 and AUC=0.91 at t=48h post sTBI. (**f-h**). Box and whisker plots represent the minima, maxima, interquartile ranges, whiskers and the median in plasma levels of the NAA levels in EC group and in patients with sTBI (relative to the HV cohort (**f, top inset**), at (**f**) t=0 (**g**) t=8h and (**h**) t=48h, representing the 25th and 75th quartiles, range and whiskers and the median with normal based, two-sided 95% confidence interval of less than ±5% for each class. At t=0, for sTBI (with sTBI+EC): n=12 and for EC: n=8, (p=0.000). At t=8h, for sTBI (with sTBI+EC): n=15 and for EC: n=8 (p=0.001). At t=48h, for sTBI (with sTBI+EC): n=11 and for EC: n=8, (p=0.002).

Fig. 4 | Rapid PoC microengineered device technology for TBI bodiagnostics. a, Neurological imaging using MRI and H^1-MRS provides stratification of TBI in a hospital environment. In the early stages post TBI, the brain leaks neuro biomarkers at very low concentrations into the CSF (Supplementary Fig. S13, c) and blood stream. A small volume of blood is collected *via* a finger prick and placed into the (**b**) optofluidic lab-on-a-chip for a rapid plasma separation schematically shown on the left hand-side. Right hand-side: an optical image of the copper master used for fabrication of the PDMS along with a zoomed-in SEM image of the micro-channel filters and reservoirs of the fabricated PDMS microfluidic chip integrated with SERS substrates , photographed on the right hand-side, functional with an input of 1-2 drops of the whole human blood (extracted by a standard pin-prick tool) to output blood plasma with operation time on the scale of 2-3 minutes and is based on the capillary motion separation approach (Supplementary Fig. S20). The microfluidics platform is ensuring a seamless integration of the substrate in the fluid flow. **c,** Schematic representation and a photograph **(inset)** of a miniaturized Raman system for multiplexed and high-throughput analyses of biomarkers. The system uses a 785nm diode laser, fed down a fibre optic and passed through a collimating lens and subsequently, the beam is reflected from a dichroic mirror down through a 20x microscope objective onto the SERS substrate. The scattered beam is reflected back up through the microscope objective lens and passes through the dichroic mirror and onto a gold coated mirror that reflects it through a lens and focuses the beam onto the slit of the spectrometer. In between the spectrometer slit and the focusing lens a 785nm edge filter is located to block the 785nm Rayleigh scattered light yet, allow the longer wavelength light through. The different wavelengths of light are then spread apart within the echelle spectrometer and collected on the cooled

CCD detector with the information being sent to a PC to display the collected spectra. **d,** The acquired SERS spectrum is rapidly compared to the pre-established finger prints of the biomarkers pool, identifying the presence of severe TBI-indicative neuro-markers (black: NAA at *t*=0, red: NAA at *t*=8h, navy: HV, *n*=12) followed by the determination of the (**e**) biomarker (NAA levels in sTBI group in comparison to HVs and the combined injury group) concentration which can be monitored over time using the integrated optofluidic chip (**inset**). The optofluidic SERS device data measured for severe TBI samples was tested for normal distribution and transformed to perform parametric tests. Comparisons across groups at each time point as well as within groups over time were performed using the analysis of variance and Tukey's *post hoc* test on the transformed data. NAA concentration was found to be significantly up-regulated in sTBI (*n*=6) and sTBI+EC (*n*=8) patients at *t*=0, compared with HV (*n*=20, *p* =0.000). sTBI (*n*=8) and sTBI+EC (*n*=10) were also found significantly upregulated compared with EC (*n*=3) at *t*=8 (*p*=0.005 and *p*=0.003, respectively) and EC *t*=48h (*n*=8, *p*=0.000).

Tables

Table 1 | Clinical characteristic and patient demographics of the studied subjects and severe TBI diagnosis. Patients were recruited from the Golden Hour and ReCoS studies. All individuals recruited were subject to two tier screening *via* the on call trauma research team at the University Hospital Birmingham. The presence of pre-morbid neurological pathology or chronic neuro degenerative pathology (including dementia, epilepsy and previous ischemic brain injury) was specific exclusion pathology, and if this was identified or suspected in the recruited patient they were excluded and samples dissuaded. The samples were obtained from a standard, widely accepted classification of the TBI severity based on clinical and neurological criteria *i.e.,* the Mayo Classification with initial clinical predictors including age, pupil reactivity, Glasgow Coma Scale (GCS), CT characteristics (Marshall CT classification) and extracranial injury (EC) as well as supported by in-hospital CT and MRI/H-MRS scans. Patients were categorised into HV, EC, sTBI and sTBI + extracranial injuries. EC injury patients had radiographically or clinically-confirmed injuries, no history or signs of head trauma and no current clinically significant infection. Individuals with a history of neurological or psychiatric disorders were excluded. Isolated sTBI patients and sTBI with EC groups included patients all with GCS≤8. All patients were gender and age matched to HVs.

Characteristics	**Traumatic Brain Injury Patients**		**EC Patients**	**Healthy Controls**
	sTBI+EC	**sTBI**		**HV**
	$n_{patients}$ =24 **$n_{samples}$= 75**	**$n_{patients}$ =11** **$n_{samples}$=37**	**$n_{patients}$ =8** **$n_{samples}$=27**	**$n_{patients}$ = 23** **$n_{samples}$=82**
Age				
Mean ±SD (Range)	47±18.8 (21-83)	40.1±16.6 (22-58)	43.6±20.6 (26-79)	42.0±15.2 (18-77)
Gender				
Male/Female	15/9	7/4	8/0	15/8
Race/Ethnicity				
White/Asian	19/5	10/1	5/3	14/9
Mechanism of Injury				
Assault/Fall	4/10	0/2	0/3	-
Penetrating/Road Traffic Accident	1/9	0/9	2/3	-
Death				
	4	1	0	-
CT Findings [a]				
Visual pathology: (-) No/(+) Yes	7/17	2/9	-	-
Clinical Diagnosis				
Marshall Grade				
Mean ±SD	**3.5 ±2.1**	**3.1 ±1.9**	-	-
Glasgow Coma Scale (GCS)				
Mean ±SD (Range)	**3.8 ±1.4 (3-8)**	**4.9 ±2 (3-8)**	-	-
Micro-engineered Technology (NAA Concentration)				
Median, *p*g/mL ±IQR	**6.73 ±4.05**	**6.03 ±0.52**	**0.85 ±0.27**	**1.22 ±0.45**

Figure 1

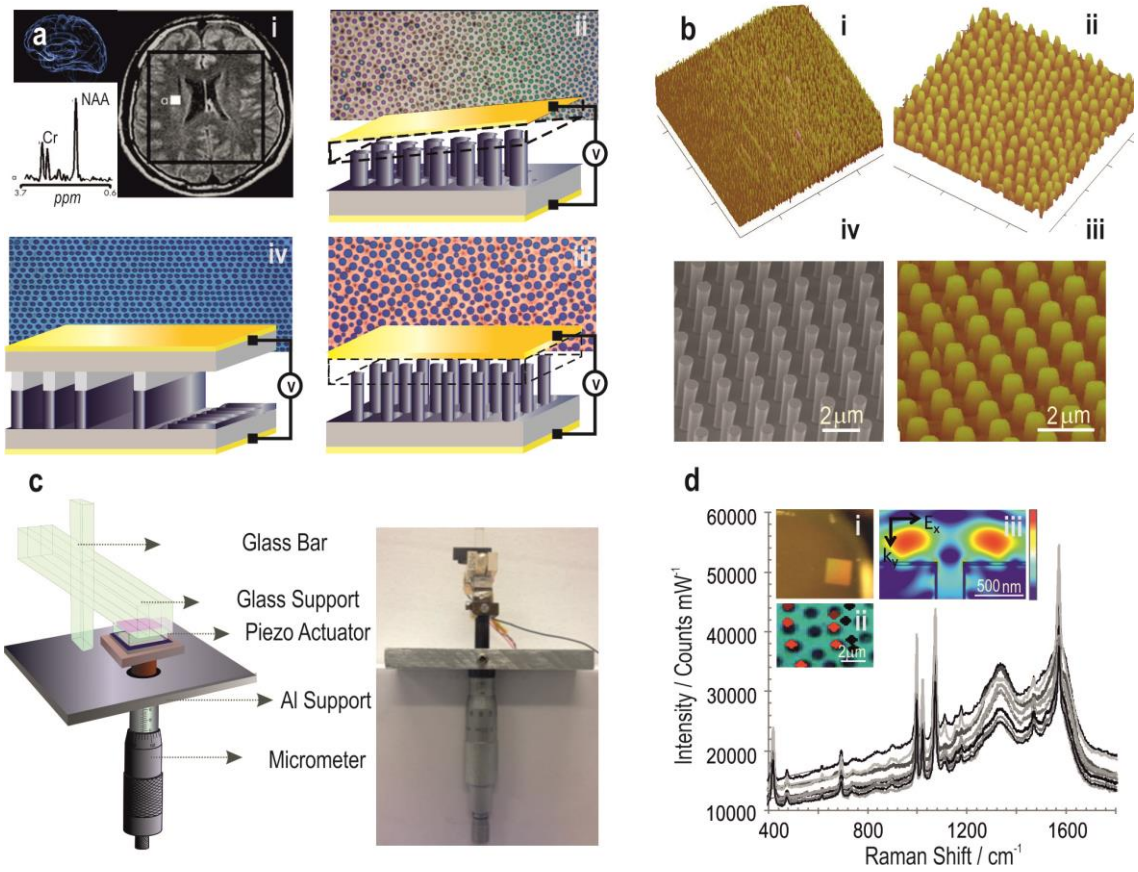

Figure 2

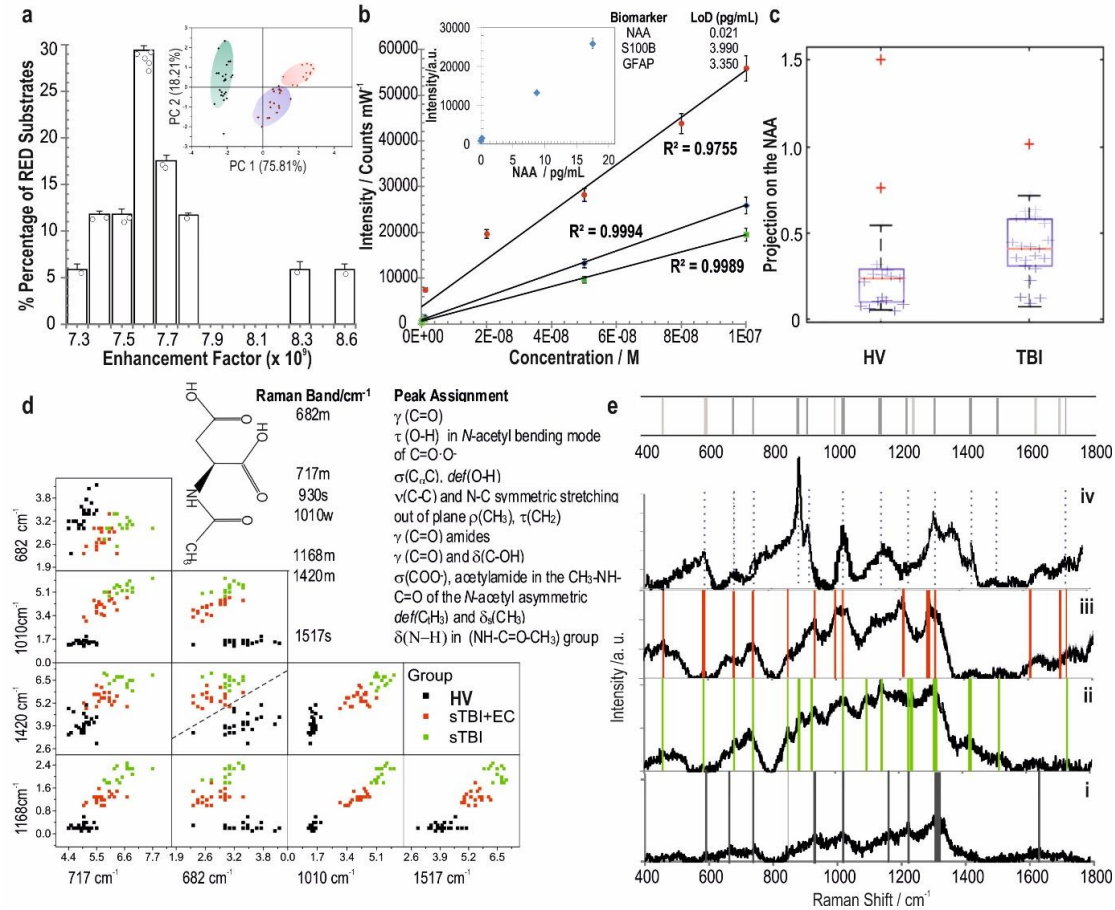

Figure 3

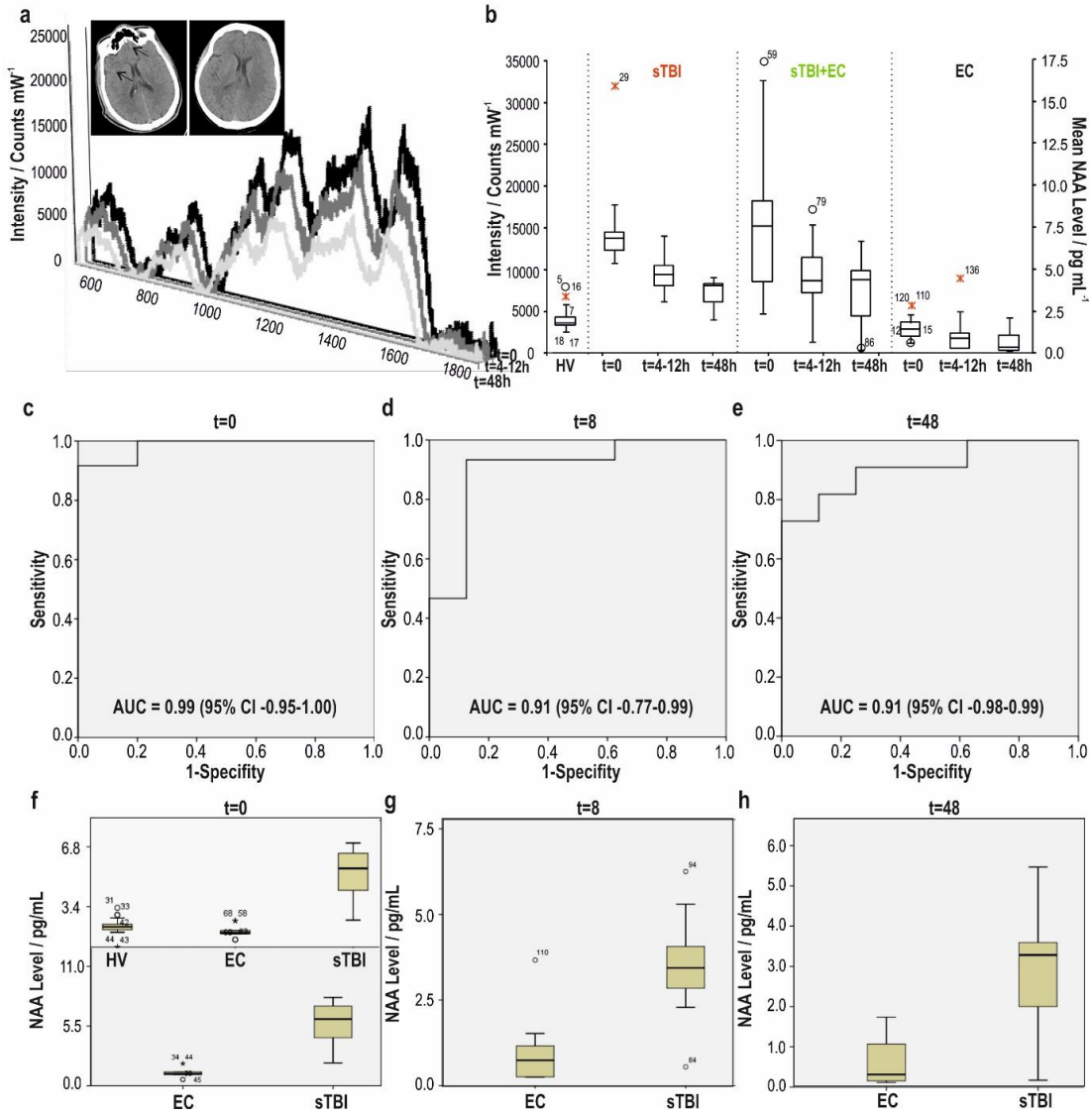

Figure 4